Title: Heterozygous expression of a *Kcnt1* gain-of-function variant has differential effects on SST- and PV-expressing cortical GABAergic neurons.

Amy N. Shore[1,2], Keyong Li[1], Mona Safari[1,3], Alshaima'a M. Qunies[4,5], Brittany D. Spitznagel[6,7,8], C. David Weaver[6,7,8], Kyle A. Emmitte[4], Wayne N. Frankel[9,10], and Matthew C. Weston[1,2,3,11*]

[1]Fralin Biomedical Research Institute at Virginia Tech Carilion, Center for Neurobiology Research, Roanoke, VA, USA.

[2]Department of Neurological Sciences, University of Vermont, Burlington, VT, USA.

[3]Translational Biology, Medicine, and Health Graduate Program, Fralin Biomedical Research Institute at Virginia Tech Carilion, Roanoke, VA, USA.

[4]Department of Pharmaceutical Sciences, UNT System College of Pharmacy, University of North Texas Health Science Center, Fort Worth, TX, USA.

[5]School of Biomedical Sciences, University of North Texas Health Science Center, Fort Worth, TX, USA.

[6]Department of Pharmacology, Vanderbilt University, Nashville, TN, USA.

[7]Vanderbilt Institute of Chemical Biology, Vanderbilt University, Nashville, TN, USA.

[8]Department of Chemistry, Vanderbilt University, Nashville, TN, USA.

[9]Institute for Genomic Medicine, Columbia University, New York, NY, USA.

[10]Department of Neurology, Columbia University, New York, NY, USA.

[11]School of Neuroscience, Virginia Tech, Blacksburg, VA, USA.

*Lead contact and correspondence: mcweston7c@vt.edu

Conflict of interest statement: The authors declare no competing financial interests.

ABSTRACT

More than twenty recurrent missense gain-of-function (GOF) mutations have been identified in the sodium-activated potassium (K_{Na}) channel gene *KCNT1* in patients with severe developmental and epileptic encephalopathies (DEEs), most of which are resistant to current therapies. Defining the neuron types most vulnerable to KCNT1 GOF will advance our understanding of disease mechanisms and provide refined targets for precision therapy efforts. Here, we assessed the effects of heterozygous expression of a *Kcnt1* GOF variant (Y777H) on K_{Na} currents and neuronal physiology among cortical glutamatergic and GABAergic neurons in mice, including those expressing vasoactive intestinal polypeptide (VIP), somatostatin (SST), and parvalbumin (PV), to identify and model the pathogenic mechanisms of autosomal dominant *KCNT1* GOF variants in DEEs. Although the *Kcnt1*-Y777H variant had no effects on glutamatergic or VIP neuron function, it increased subthreshold K_{Na} currents in both SST and PV neurons but with opposite effects on neuronal output; SST neurons became hypoexcitable with a higher rheobase current and lower action potential (AP) firing frequency, whereas PV neurons became hyperexcitable with a lower rheobase current and higher AP firing frequency. Further neurophysiological and computational modeling experiments showed that the differential effects of the Y777H variant on SST and PV neurons are not likely due to inherent differences in these neuron types, but to an increased persistent sodium current in PV, but not SST, neurons. The Y777H variant also increased excitatory input onto, and chemical and electrical synaptic connectivity between, SST neurons. Together, these data suggest differential pathogenic mechanisms, both direct and compensatory, contribute to disease phenotypes, and provide a salient example of how a pathogenic ion channel variant can cause opposite functional effects in closely related neuron subtypes due to interactions with other ionic conductances.

Keywords: epilepsy; DEE; ADNFLE; KCNT1 channel; Slack; K_{Na} current; potassium channel; GOF variant; glutamatergic; GABAergic; SST; PV; VIP; electrophysiology

INTRODUCTION

Heterozygous missense variants have been identified in the sodium-gated potassium channel gene *KCNT1* in more than 200 individuals exhibiting a wide spectrum of developmental and epileptic encephalopathies (DEEs), with the majority being classified as either epilepsy of infancy with migrating focal seizures (EIMFS) or autosomal dominant or sporadic sleep-related hypermotor epilepsy (ADSHE) (Barcia et al., 2012; Bonardi et al., 2021; Heron et al., 2012). Each of these epilepsy syndromes result in early-onset, frequent seizures that are largely pharmacoresistant and often accompanied by a range of cognitive, psychiatric, and motor impairments. Thus, there is a critical need for a better understanding of how heterozygous expression of these *KCNT1* variants in the developing brain alters neuronal physiology and network behavior to lead to such devastating neurodevelopmental disorders.

KCNT1 encodes a tetrameric potassium channel that is widely expressed in both glutamatergic and GABAergic neurons of the brain, particularly those of the cerebellum, striatum, thalamus, hippocampus, and cortex (Berg et al., 2007; Bhattacharjee et al., 2002; Gertler et al., 2022; Rizzi et al., 2016). Although its precise role in normal physiology is not well understood, at least in some neuronal types, KCNT1 is activated by a persistent inward sodium leak (Na_P) current at rest, where it has a proposed role in fine tuning neuronal excitability by countering the effects of the Na_P current across subthreshold voltages (Budelli et al., 2009; Hage & Salkoff, 2012). Consistent with this role, loss-of-function (LOF) studies using mouse models lacking KCNT1, and the associated sodium-activated potassium (K_{Na}) current, have shown enhanced AP firing across multiple neuron types (Evely et al., 2017; Liu et al., 2022; Lu et al., 2015; Martinez-Espinosa et al., 2015; Reijntjes et al., 2019; Zhang et al., 2022). Characterizations of pathogenic DEE-associated *KCNT1* variants in heterologous cells found that nearly all cause gain-of-function (GOF) effects on the channel, increasing the associated K_{Na} current (Hinckley et al., 2023; Kim et al., 2014; McTague et al., 2018; Milligan et al., 2014; Tang et al., 2016). Based on LOF studies, this would be expected to reduce neuronal excitability; however, it is difficult to predict the

effects of these GOF variants on AP generation in neurons, particularly among neuronal subtypes, *a priori*.

To address this knowledge gap, we previously generated and characterized a mouse model expressing a human ADNFLE-associated *KCNT1* GOF variant (Y796H, or Y777H in mice) (Shore et al., 2020). Although heterozygous expression of the *KCNT1*-Y796H variant is sufficient to cause severe childhood epilepsy in humans, we only observed rare behavioral seizures in heterozygous *Kcnt1*-Y777H mice [see Discussion-(Shore et al., 2020)]; however, we identified hyperexcitable, hypersynchronous cortical networks and frequent, early-onset seizures in homozygous *Kcnt1*-Y777H mice. As a potential underlying mechanism of these network alterations, we demonstrated that homozygous *Kcnt1*-Y777H expression increases subthreshold K_{Na} currents and reduces excitability in GABAergic neuron populations, particularly in those classified as non-fast spiking (NFS), but it does not alter glutamatergic neuron excitability. We further observed evidence of homeostatic compensation and network remodeling downstream of K_{Na} current increases during development, including increased excitatory input onto glutamatergic and NFS GABAergic neurons, and enhanced homotypic synaptic connectivity. Although these findings provide a strong mechanistic basis for understanding how KCNT1 GOF disrupts neuronal physiology and network behavior to lead to seizure disorders, key issues remain unresolved. First, considering the heterozygous nature of *KCNT1* GOF variants in the overwhelming majority of *KCNT1*-related DEE patients, it is crucial to determine whether heterozygous *Kcnt1*-Y777H expression results in similar neuronal impairments and network alterations to those with homozygous expression. Second, more recent studies, using both *in silico* modeling and additional construct-valid mouse models, have similarly identified impairments in GABAergic neuron excitability downstream of KCNT1 GOF (Gertler et al., 2022; Kuchenbuch et al., 2021; Wu et al., 2024), indicating impaired inhibition as a shared pathogenic mechanism in *KCNT1*-related DEEs; however, precisely which GABAergic subtypes are most impacted, and how, remains unknown.

Here, we assessed the effects of heterozygous *Kcnt1*-Y777H expression on K_{Na} currents and neuronal physiology among cortical glutamatergic and GABAergic neurons, including those expressing vasoactive intestinal polypeptide (VIP), somatostatin (SST), and parvalbumin (PV). Initial assessments of cortical neuron populations with heterozygous Y777H expression showed strikingly similar effects on K_{Na} currents and AP generation to those with homozygous expression, although not surprisingly, these effects were lesser in magnitude. Across all cortical neuron types examined, the heterozygous *Kcnt1*-Y777H variant caused a range of effects on neuronal excitability and action potential (AP) generation, from no change (glutamatergic and VIP GABAergic) to decreased excitability (SST GABAergic) to increased excitability (PV GABAergic). Neuron types that showed no change had K_{Na} currents that were only significantly increased at suprathreshold voltages and exhibited a steeper voltage dependence of activation. Interestingly, both SST and PV neurons showed similar increases in K_{Na} currents across subthreshold voltages, however, only PV neurons had additional increases in the persistent Na^+ current, which modeling experiments indicated was sufficient to overcome the effects of KCNT1 GOF and cause an overall increase in AP generation. SST neurons also showed an increase in excitatory input, and in homotypic electrical and chemical coupling. Taken together, these data provide further evidence of the enhanced vulnerability of GABAergic neurons, particularly those expressing SST and PV, to KCNT1 GOF. Moreover, these data show that heterozygous expression of a single *KCNT1* GOF variant can result in a complex array of neuron type-dependent effects, both direct and indirect, each potential contributors to the neural circuit pathology underlying *KCNT1*-related DEEs.

RESULTS

Heterozygous *Kcnt1*-Y777H expression alters the shape and frequency of APs in NFS GABAergic neurons.

We previously identified frequent, early-onset seizures in mice with homozygous expression of the *Kcnt1* GOF variant Y777H (hereafter referred to as YH-HOM), and as a potential underlying pathological mechanism, we demonstrated that homozygous *Kcnt1*-Y777H expression drastically impairs action potential (AP) shape and generation in non-fast spiking (NFS) GABAergic cortical neurons, with lesser effects on fast spiking (FS) GABAergic, and no significant effects on glutamatergic, cortical neurons (Shore et al., 2020). Considering that patients with *KCNT1*-associated epilepsy are predominantly heterozygous for *KCNT1* GOF variants, it is crucial to determine whether heterozygous expression of these variants, which likely leads to the formation of heteromeric channels consisting of WT and mutant subunits, results in similar neuronal impairments. To assess neuron subtype-specific effects of heterozygous KCNT1 GOF on membrane properties and AP firing, we isolated and cultured cortical neurons from pups with heterozygous Kcnt1-Y777H expression (hereafter referred to as YH-HET), and their WT littermates, at postnatal day 0 (P0). After infecting the cultured neurons with AAV-*CaMKII*-GFP to facilitate glutamatergic neuron identification, we performed whole-cell, current-clamp analysis between 13 and 17 days *in vitro* (DIV). Moreover, to compare to homozygous KCNT1 GOF effects observed previously, the recorded neurons were classified as glutamatergic, FS GABAergic, or NFS GABAergic, based on GFP expression, AP parameters, and evoked synaptic responses (see Methods).

Current-clamp recordings from YH-HET and WT glutamatergic neurons showed no significant differences in any membrane or AP shape property measured (Fig. $1A_1$ and Supplemental Table 1), similar to observations from the homozygous KCNT1 GOF studies. Accordingly, AP firing frequencies across increasing current steps in YH-HET glutamatergic neurons were not altered compared with those of WT (Fig. $1B_1$). For FS GABAergic neurons, we previously showed that homozygous Y777H expression increases the rheobase—the minimal amount of current necessary to induce an AP—and reduces the AP firing frequency. Heterozygous Y777H expression did not alter the rheobase, or any other passive or active membrane property of FS GABAergic neurons (Fig. $1A_2$ and Supplemental Table 1). Although YH-

HET FS GABAergic neurons appeared to fire fewer APs than their WT counterparts, particularly at higher current steps, this effect was not significant (Fig. $1B_2$). Lastly, we previously showed that homozygous Y777H expression has the strongest effects in NFS GABAergic neurons, showing a decrease in input resistance, accompanied by an increase in rheobase and a reduction in AP firing frequency. YH-HOM NFS GABAergic neurons also have narrower AP half-widths and larger afterhyperpolarizations (AHPs) than those of WT. Although heterozygous Y777H expression in NFS GABAergic neurons did not cause a significant decrease in input resistance (WT: 171 ± 16; YH-HET: 146 ± 14, p=0.19), it did increase the rheobase and reduce the AP firing frequency, particularly at lower current steps, relative to those of WT (Fig. $1A_3$ and $1B_3$). YH-HET NFS GABAergic neurons also had narrower APs, larger AHPs, and more depolarized AP thresholds than those of WT (Supplemental Table 1). Together, these data demonstrate that the neurophysiological effects on cortical neurons with monoallelic expression of the *Kcnt1*-Y777H variant, expressing channels with mutant and WT subunits, are similar to those with biallelic expression, expressing only mutant subunits, with both causing the strongest impairments in NFS GABAergic neurons.

Heterozygous *Kcnt1*-Y777H expression increases subthreshold K_{Na} currents in NFS GABAergic neurons.

Previously, we showed that homozygous *Kcnt1*-Y777H expression in GABAergic cortical neurons increases the K_{Na} current across subthreshold voltages, an effect that is particularly evident in NFS GABAergic neurons; conversely, in glutamatergic cortical neurons with homozygous expression of the same variant, increases in K_{Na} currents are only apparent at depolarized voltages (> +30 mV) (Shore et al., 2020). To assess the effects of heterozygous Y777H expression on KCNT1 channel function, we measured the associated K_{Na} current in each cortical neuron subtype. We recorded K_{Na} currents by applying voltage steps to voltage-clamped neurons and comparing the delayed outward current before and after the addition of the voltage-gated sodium channel inhibitor TTX (Fig. $2A_{1\text{-}3}$). As reported

previously, there were K_{Na} currents in all three WT neuron subtypes, beginning around -10 mV and increasing with depolarization (Fig. $2A_{1-3}$ and $2B_{1-3}$), whereas at more negative potentials, the TTX-sensitive current was net inward (Fig. $2C_{1-3}$) due to the counteracting persistent Na^+ current.

In glutamatergic and NFS GABAergic YH-HET neurons, the overall K_{Na} current was increased relative to those of WT, as measured by a significant effect of genotype using a linear model (Fig. $2B_{1,3}$). Importantly, in each of these neuron subtypes, heterozygous Y777H expression increased K_{Na} currents with distinct, voltage-dependent patterns that appeared strikingly similar to those reported with homozygous expression. For instance, we previously showed that, across negative potentials, YH-HOM and WT glutamatergic neuron K_{Na} currents are indistinguishable, whereas at more positive potentials (> +30 mV), the Y777H variant causes significant increases in K_{Na} currents. Similar voltage-dependent effects were observed in YH-HET glutamatergic neurons (Fig. $2B_1$ and $2C_1$), although pairwise comparisons showed that K_{Na} current increases at positive potentials in the YH-HET glutamatergic neurons were not significant. Conversely, we previously demonstrated broad increases in K_{Na} currents across negative potentials, with significant increases from -60 to +10 mV, in YH-HOM NFS GABAergic neurons compared with those of WT, with lesser effects across positive potentials. Similar voltage-dependent increases were observed in YH-HET NFS GABAergic neurons, with pairwise comparisons showing significant K_{Na} current increases at -70, -60, -50, and -20 mV (Fig. $2B_3$ and $2C_3$). For both glutamatergic and NFS GABAergic neurons, the magnitudes of the K_{Na} current increases in YH-HET neurons were intermediate to those of WT and YH-HOM neurons (Supplemental Fig. 2-1), demonstrating a gene dose-dependent effect of the *Kcnt1*-Y777H variant on K_{Na} current increases and validating a GOF effect of the heterozygous Y777H variant on channel function. Lastly, although previous studies showed that homozygous Y777H expression increases K_{Na} current at several negative voltage steps (-50, -40, and -10 mV) in FS GABAergic neurons, heterozygous expression of the same variant in FS

GABAergic neurons caused no significant differences in K_{Na} currents compared with those of WT (Fig. $2B_2$ and $2C_2$).

Heterozygous *Kcnt1*-Y777H expression does not alter synaptic connectivity or the excitation-inhibition balance.

In addition to alterations in the intrinsic passive and active membrane properties of cortical neurons with homozygous Y777H expression, we previously showed evidence of altered synaptic connectivity and activity, leading to hypersynchronous, hyperexcitable YH-HOM networks; more specifically, we found an increase in homotypic coupling between glutamatergic [excitatory–excitatory (E–E)] and GABAergic [inhibitory–inhibitory (I–I)] neuron pairs, and an increase in the frequency of spontaneous excitatory postsynaptic currents (sEPSCs), accompanied by an increase in the E/I ratio, onto YH-HOM glutamatergic cortical neurons (Shore et al., 2020). First, to determine whether there are similar changes in synaptic connectivity in YH-HET networks, we performed paired recordings of glutamatergic (excitatory, E) and GABAergic (inhibitory, I) neurons and alternatively stimulated each neuron at 0.1 Hz to test baseline connection probability and strength at the four possible motifs (E–E, I–E, E–I, and I–I). Connection probability was not altered in YH-HET networks at any of the motifs tested (Fig. $3A_{1\text{-}4}$, left bar graphs), and the amplitudes of the evoked postsynaptic currents (ePSCs) between connected neurons were not different between genotypes for any of the four connection types (Fig. $3A_{1\text{-}4}$, right bar graphs), indicating grossly normal synaptic interactions among glutamatergic and GABAergic neurons in YH-HET networks. Next, to assess potential alterations in synaptic activity, we recorded spontaneous postsynaptic currents (sEPSCs and sIPSCs) onto voltage-clamped glutamatergic and GABAergic neurons. Unlike the observation of an increase in sEPSC frequency onto YH-HOM glutamatergic neurons, there was no difference in sEPSC, or sIPSC, frequency onto YH-HET glutamatergic neurons (Fig. $3B_1$). Furthermore, although we previously found no alterations in sPSC frequency onto

YH-HOM GABAergic neurons, sEPSC and sIPSC frequencies were both slightly reduced onto YH-HET GABAergic neurons (Fig. $3B_2$). Finally, to assess the net effect of altered sPSC activity onto YH-HET neurons, we calculated the E/I ratio, based on the relative frequency and size of the sPSCs, and found no difference in the E/I ratio onto either YH-HET neuron type (Fig. $3B_3$). Thus, although heterozygous Y777H expression resulted in similar K_{Na} current increases and neuronal physiology effects to those found with homozygous Y777H expression, the broad effects on synaptic connectivity and activity found in YH-HOM networks were absent in YH-HET networks, which likely results in the observed reduction in seizure incidence in heterozygous, relative to homozygous, mice.

Heterozygous *Kcnt1*-Y777H expression differentially affects the intrinsic excitability of SST- and PV-expressing GABAergic neurons.

Next, we sought to determine which GABAergic subtypes are most impacted by heterozygous Kcnt1-Y777H expression. About 80–90% of cortical GABAergic neurons fall into three, largely non-overlapping populations that can be identified by their expression of unique markers: the Ca^{2+}-binding protein parvalbumin (PV; ~40%) and the neuropeptides somatostatin (SST; ~30%) and vasoactive intestinal polypeptide (VIP; ~15%) (Rudy et al., 2011; Tremblay et al., 2016). The majority of PV-expressing neurons have been characterized as FS, and VIP-expressing as NFS, whereas SST-expressing neurons, although largely thought to show NFS firing properties, also contain a population that exhibits a FS-like phenotype (Large et al., 2016; Ma et al., 2006). *KCNT1* is expressed at higher levels in both human and mouse cortical GABAergic neurons expressing PV and SST, than in those expressing VIP (Gertler et al., 2022; Shore et al., 2020). Based on the expression profile of KCNT1, and our findings that homozygous and heterozygous expression of the *Kcnt1* GOF variant strongly reduced the excitability GABAergic neurons with NFS firing properties, we hypothesized that the SST-expressing neurons are the most vulnerable to the effects of KCNT1 GOF. To test this hypothesis, we crossed PV-, SST-, and VIP-Cre

mouse lines to the *Kcnt1*-Y777H mouse line and cultured neurons from the cortices of WT and YH-HET littermate progeny (Fig. 4A and Supplemental Fig. 4-1A). We infected the cultured neurons with AAV-*CaMKII*-GFP, to mark glutamatergic neurons, and AAV-*hSyn*-DIO-mCherry, to mark Cre recombinase-expressing GABAergic neurons, and performed whole-cell, patch-clamp electrophysiology at DIV 13–17 on GFP^-/$mCherry^+$ neurons from each group.

First, we measured the intrinsic membrane properties and AP shape parameters of the three GABAergic subtypes from the WT control groups to verify that they accurately reflected electrophysiological behaviors of these subtypes from previous *ex vivo* recordings (Taniguchi et al., 2011). As expected, the VIP neurons showed a relatively large input resistance, small rheobase, wide AP half-width, small AHP, and low firing rate (Supplemental Fig. 4-1B and 4-1C, purple); in contrast, PV neurons showed a small input resistance, large rheobase, narrow AP half-width, large AHP, and high firing rate (Supplemental Fig. 4-1B and 4-1C, orange). For SST neurons, the values measured for input resistance, rheobase, AP half-width, AHP, and firing rate were all intermediate to those of VIP and PV neurons (Supplemental Fig. 4-1B and 4-1C, blue). Moreover, as reported previously, SST neurons showed the most hyperpolarized AP threshold of the three groups. Together, these data demonstrate the ability of cortical GABAergic neuron subtypes to retain their characteristic *ex vivo* passive and active membrane properties *in vitro*.

Next, we assessed the effects of the Y777H variant on the passive and active membrane properties of each GABAergic subtype. Current-clamp recordings from YH-HET VIP neurons revealed no significant effect of the variant on any of the membrane or AP properties measured (Fig. $4B_1$). Conversely, YH-HET SST neurons showed a strong decrease in input resistance, with an accompanying increase in rheobase current, relative to those of WT SST neurons (Fig. $4B_2$), similar to the hypoexcitable membrane phenotype observed in the YH-HET NFS neurons, without altering AP shape parameters. YH-HET SST neurons also showed a reduction in the membrane time constant and an increase in membrane

capacitance, which was accompanied by an increase in soma size (Supplemental Table 4 and Supplemental Fig. 4-2), compared with those of WT SST neurons. Unexpectedly, YH-HET PV neurons exhibited a decrease in the rheobase current compared with that of WT (Fig. $4B_3$), and an increase in AP amplitude (Supplemental Table 4), suggesting the Y777H variant increases PV neuron excitability.

Next, we measured AP firing frequency with incremental, 500-ms current steps in each of the three GABAergic subtypes. WT neurons showed AP firing frequencies similar to those reported previously from *ex vivo* recordings of neurons from the three Cre lines (Taniguchi et al., 2011), with VIP showing the lowest maximal firing frequency, PV the highest, and SST intermediate between VIP and PV (Fig. $4C_{1\text{-}3}$ and Supplemental Table 4). Consistent with a lack of any effects on membrane and AP shape properties, the AP firing frequencies across increasing current steps were indistinguishable between WT and YH-HET VIP neurons (Fig. $4C_1$). As expected, based on their hypoexcitable membrane properties, the YH-HET SST neurons fired fewer APs across all current steps relative to WT SST neurons (Fig. $4C_2$). In contrast to SST neurons, but consistent with their decreased rheobase current, YH-HET PV neurons fired more APs across all current steps relative to their WT counterparts (Fig. $4C_3$). Notably, although these experiments were performed at room temperature (~22°C), and increasing temperatures to 35°C altered multiple neuronal physiology parameters (Supplemental Fig. 4-3A), both WT and YH-HET PV neurons responded similarly to increased temperature (Supplemental Fig. 4-3B), suggesting that the observed phenotypes are not temperature dependent. Together, these data showed that, as hypothesized, KCNT1 GOF indeed strongly reduces the excitability of SST neurons, but unexpectedly, it also causes a hyperexcitable effect in PV neurons; thus, the same ion channel mutation can lead to opposite effects on excitability in the two largest GABAergic neuron subtypes.

The Y777H variant increases KCNT1-mediated currents across subthreshold voltages in SST- and PV-expressing GABAergic neurons.

Are the observed differential effects of KCNT1 GOF on GABAergic neuronal physiology due to distinct patterns of K_{Na} current increases among GABAergic neuron subtypes? To answer this question, we first recorded K_{Na} currents from GABAergic neurons cultured and labeled as described above, by applying voltage steps to voltage-clamped neurons and comparing the delayed outward current before and after the addition of TTX (Supplemental Fig. 5-1A_{1-3}). In all three subtypes, for both WT and YH-HET neurons, we observed K_{Na} currents beginning around -10 mV and increasing with depolarization (Supplemental Fig. 5-1B_{1-3}). For YH-HET VIP neurons, pairwise comparisons to assess voltage-dependent differences showed that their K_{Na} currents were not different from those of WT at any voltage step (Supplemental Fig. 5-1B_1 and 5-1C_1). On the other hand, YH-HET SST neurons showed significant increases in K_{Na} currents compared with those of WT across multiple subthreshold voltage steps, including -60, -50, and -40 mV (Supplemental Fig. 5-1B_2 and 5-1C_2), similar to those observed in NFS GABAergic neurons with both heterozygous (Fig. 2) and homozygous expression of the Y777H variant (Shore et al., 2020), indicating a direct current-to-phenotype relationship in YH-HET SST neurons. Somewhat unexpectedly, pairwise comparisons showed that K_{Na} currents were not different between YH-HET and WT PV neurons at any voltage step (Supplemental Fig. 5-1B_3 and 5-1C_3).

The lack of an increase in TTX-sensitive currents in PV neurons, despite alterations in rheobase, AP amplitude, and AP firing frequency, suggests that either a TTX-insensitive Na^+ source activates KCNT1, or that compensatory alterations in an opposing current mask an increase in K_{Na} and lead to the changes in AP firing. In past studies, the lack of selective KCNT1-specific inhibitors necessitated the use of indirect methods, such as TTX application or Na^+ replacement, to estimate the magnitude of K_{Na}. However, more recently, we identified and validated a small-molecule, selective KCNT1 channel inhibitor termed VU0606170, or VU170 (Spitznagel et al., 2020). To further validate the specificity of this small molecule, we applied voltage steps to voltage-clamped neurons lacking KCNT1 and KCNT2 channels, isolated and cultured from *Kcnt1*$^{-/-}$; *Kcnt2*$^{-/-}$ double knockout mice (Martinez-Espinosa et al., 2015), and we compared

the delayed outward current before and after the addition of either 10 µM VU170 or 0.5 µM TTX. This analysis indicated a non-specific outward VU-sensitive current that started around -10 mV and peaked at +50 mV (~1 nA peak current compared with ~3 nA in WT neurons), which was not present using TTX subtraction (Supplemental Fig. 5-2A). Across negative potentials, there was an inward TTX-sensitive current, which again is likely due to the persistent Na^+ current, whereas there was little to no outward VU-sensitive current (Supplemental Fig. 5-2B), validating the utility of VU170 in isolating K_{Na} currents across this voltage range.

To better assess KCNT1-mediated currents in GABAergic subpopulations and disentangle potential confounds of using TTX, particularly across negative potentials, we applied the same voltage step protocol as in the TTX subtraction experiments but applied 10 µM VU170 instead. In all three WT GABAergic neuron subtypes, subtraction of the VU170 trace from the control trace revealed nA-sized outward currents at depolarized potentials, and in YH-HET neurons, the overall VU170-sensitive current was increased relative to those of WT, as measured by a significant effect of genotype using a linear model (Fig. $5A_{1-3}$ and $5B_{1-3}$). Pairwise comparisons at each voltage step showed voltage-dependent differences in current increases among the YH-HET neuron subtypes. For YH-HET VIP neurons, a significant increase in the VU170 current was only observed at +50 mV (Fig. $5B_1$), whereas subthreshold currents were indistinguishable from those of WT (Fig. $5C_1$). Previously, we similarly observed K_{Na} current increases only at more positive potentials in YH-HOM glutamatergic neurons, and like YH-HET VIP neurons, their membrane and AP properties were unaltered by expression of the YH variant (Shore et al., 2020). Conversely, in YH-HET SST neurons, significant increases occurred at more negative voltage steps, from -60 to -30 mV (Fig. $5C_2$). These changes were similar to those observed with TTX treatment, but slightly larger, possibly due to the lack of the counteracting effect of the persistent Na^+ current, which is also blocked by TTX. In contrast to the TTX results, YH-HET PV neurons showed an increase in VU170-sensitive currents, with significant increases from -70 to -50 mV (Fig. $5C_3$). Taken together, these

data identify distinct patterns of K_{Na} current increases among GABAergic subtypes, and for VIP and SST neurons, these current increases are consistent with the observed effects of KCNT1 GOF on neuronal physiology. On the other hand, PV neurons showed subthreshold-specific K_{Na} current increases that were highly similar to, and overlapping with, those of SST neurons; thus, differential K_{Na} current increases alone likely do not account for the opposite effects of KCNT1 GOF on physiology observed in these two neuron types.

Compartmental models of KCNT1 GOF in SST, but not PV, neurons are consistent with experimental data.

The VU170-subtraction experiments showed that YH-HET SST and PV neurons have similar subthreshold increases in KCNT1-mediated currents, even though they exhibited opposing effects on neuron excitability and AP generation, and that YH-HET VIP neurons have suprathreshold increases in KCNT1-mediated currents with no effects on neuron physiology. Because GABAergic subtypes exhibit varying morphologies and express unique repertoires of ion channels, which are known to give rise to their characteristic membrane and AP firing properties, we hypothesized that at least some of the observed differential effects of KCNT1 GOF, in particular the opposite effects in SST and PV neurons, are due to these inherent, neuron-type-dependent differences. To test this hypothesis, we simulated the effect of KCNT1 GOF in compartmental models of these three cortical neuron types. We used a KCNT1 conductance with the Na^+ dependence constrained by prior studies in neurons (EC_{50} = 40 mM, slope 3.5; see Materials and Methods) and the voltage dependence based on the activation curves from our own experimental data of the VU170-sensitive current in each subtype (Fig. 6A). The kinetics of the model current were set by measuring the onset time course of the VU170-sensitive current in outside-out membrane patches of each neuron type (Fig. 6B and 6C). This conductance was inserted into compartmental models of 10 neurons per subtype, representing a variety of morphological and

electrical properties of each subtype (Markram et al., 2015). Because the Y796H variant was previously shown to increase the Na^+ sensitivity of the channel, we modeled the GOF effect by reducing the EC_{50} for Na^+ activation to two levels (35 mM and 30 mM), which resulted in moderate K_{Na} current increases above WT levels (Fig. 6D).

Consistent with our experimental data, introducing KCNT1 GOF at the lower level (EC_{50} = 35 mM) into model VIP neurons did not alter their AP firing rate, input resistance, or rheobase, whereas at the higher level (EC_{50} = 30 mM), there were small changes in input resistance (40 mM: 266.5 ± 28.2; 30 mM: 264.8 ± 28.0, p=0.012) and rheobase (40 mM: 78.7 ± 11.6; 30 mM: 80.4 ± 11.1, p=0.014), but these changes were not sufficient to affect the AP firing rate (Fig. $6E_1$ and $6E_2$, Supplemental Table 6, and Supplemental Fig. 6-2A). On the other hand, model SST neurons with KCNT1 GOF at both levels fired fewer APs per current step as the GOF was increased, and showed significantly reduced input resistances, higher rheobases, and lower AP firing rates (Fig. $6F_1$ and $6F_2$, Supplemental Table 6), results that agree with our experimental observations. In contrast to experimental data, but similar to model SST neurons, model PV neurons responded to KCNT1 GOF with decreased input resistance, increased rheobase, and a reduced AP firing rate (Fig. $6G_1$ and $6G_2$ and Supplemental Table 6), although the magnitude of these effects were smaller than those in model SST neurons (Supplemental Fig. 6-2A). These data suggest that the increased excitability observed in YH-HET PV neurons is not simply due to an intrinsic property of this GABAergic subtype, but instead results from an indirect mechanism (e.g. a compensatory response like an increase in Na^+ channels) or depends on a feature of KCNT1 function not captured by the model.

Lastly, we hypothesized that the lack of GOF effects on VIP and glutamatergic neuron physiology is due to the altered kinetics of their KCNT1 channel activation curves, in particular their right shifted V_{50} and decreased slope, relative to those of SST or PV neurons (Fig. 6A). To test this hypothesis, we performed simulations in which the activation curve parameters (V_{50} and slope) measured in SST

neurons were inserted into VIP and glutamatergic neurons, with the Na^+ EC_{50} set to 30 mM to simulate KCNT1 GOF (Supplemental Fig. 6-1A_1 and 6-1B_1, blue traces). Inserting KCNT1 channels with SST kinetics into VIP and glutamatergic neurons indeed enhanced the GOF effects on input resistance and rheobase, and importantly, resulted in a significantly decreased AP firing rate relative to control neurons for both neuron types (Supplemental Fig. 6-1A_2 and 6-1B_2, Supplemental Table 6, and Supplemental Fig. 6-2B). This model-based evidence suggests that the relative sensitivity of SST and PV neurons, and resistance of VIP and glutamatergic neurons, to KCNT1 GOF is due to the differences in voltage dependence of the K_{Na} current in each subtype.

The persistent Na^+ current is increased by the *Kcnt1*-Y777H variant in PV, but not SST, neurons.

The modeling results suggest that a subthreshold increase in the K_{Na} current alone is not sufficient to account for the alterations in PV neuron excitability. Moreover, the finding of an increase in the KCNT1-mediated current in YH-HET PV neurons when measured with VU170, but not TTX, isolation suggests there may be a compensatory upregulation of an opposing current that masks the increase in K_{Na} and leads to the unexplained increase in AP firing. The persistent Na^+ current (I_{NaP}) is active on the same time scale as K_{Na} and was previously shown to provide the Na^+ source for K_{Na} (Hage & Salkoff, 2012); therefore, we hypothesized that KCNT1 GOF causes an increase in I_{NaP} in PV neurons that enhances their excitability. To test this hypothesis, we measured I_{NaP} in SST and PV neurons by applying TTX during slow voltage ramp protocols (20 mV/s) designed to isolate I_{NaP} from both the transient Na^+ current and the K_{Na} current (Supplemental Fig. 7-1).

In SST neurons, I_{NaP} did not differ between WT and YH-HET neurons, either in the shape of the response (Fig. 7A and 7B), or the peak amplitude (Fig. 7B). In PV neurons, however, the peak amplitude of I_{NaP} was significantly increased by the Y777H variant (Fig. 7C and 7D). Interestingly, the mean peak amplitude of I_{NaP} in WT PV neurons was 70% larger than that in WT SST neurons (-1.42 ± 0.16 vs. -0.85 ±

0.07 pA/pF; Fig. 7B and 7D), suggesting there may be differences in sodium channel expression, localization, or regulation inherent to each neuron type that confer their differential response to KCNT1 GOF. To examine whether the observed increase in I_{NaP} in YH-HET PV neurons could account for the increase in AP firing, we again simulated the effect of KCNT1 GOF (Na^+ EC_{50} = 35 mM) on PV neuron activity, but this time included an increase in I_{NaP} in the compartmental models. Indeed, an increase in I_{NaP} conductance, similar to what was seen in the experimental results (2-fold), was sufficient to increase the number of APs fired in response to increasing current steps (Fig. 7E and 7F and Supplemental Table 6), even in the face of the higher level of KCNT1 GOF (30 mM; Supplemental Table 6 and Supplemental Fig. 7-2). Also, like the experimental data, the rheobase current was decreased (Fig. 7F and Supplemental Fig. 7-2) and the AP height was increased (80.4 ± 0.7 vs. 82.1 ± 0.8 mV). These results suggest that the differential effects on AP firing in SST and PV neurons can be accounted for by the absence or presence of a secondary increase in I_{NaP}.

YH-HET SST neurons show increased chemical and electrical coupling and receive increased excitatory input.

We previously showed that homozygous expression of the Y777H variant increased connections between GABAergic neurons (Shore et al., 2020), but heterozygous expression did not (Fig. 3). Because heterozygous Y777H variant expression caused the strongest excitability impairments in SST neurons, we hypothesized that alterations in synaptic connectivity and activity may be more likely to occur in this neuronal population. To test this hypothesis, we recorded from pairs of WT or YH-HET SST neurons as described above to measure connection probability and strength. Indeed, similar to the increase observed in I–I connections in YH-HOM networks, we found an increase in homotypic synaptic connections of SST neurons in YH-HET networks (30/40 connections) relative to those in WT (15/40

connections; Fig. 8A). The amplitudes of the evoked postsynaptic currents (ePSCs) between connected SST neurons were not significantly different between the YH-HET and WT groups (Fig. 8B).

There are two main types of synaptic coupling between neurons: chemical, which is mediated by neurotransmitter release, and electrical, which is mediated by gap junctions. To test for alterations in each type of synaptic coupling due to expression of the *Kcnt1* variant, we recorded from 20 pairs of WT or YH-HET SST neurons in close proximity (< 100 µm apart). Under current-clamp conditions, we injected a series of hyperpolarizing and depolarizing current steps into one neuron and assessed whether the current induced a simultaneous voltage deflection in the paired, non-injected neuron (Fig.8C_1; 100-pA-evoked response). We then evoked a train of APs in one neuron and assessed the AP-induced voltage changes in the paired, non-injected neuron (Fig. 8C_1; AP-evoked response). SST pairs were considered to be chemically coupled if the AP trains in one neuron induced corresponding IPSCs, without inducing voltage deflections in response to the current steps, onto the paired neuron (Fig. 8C_1; top panels). SST pairs were considered to be electrically coupled if the current steps injected into one neuron induced simultaneous voltage deflections in the paired neuron (Fig. 8C_1; bottom panel, left). Electrically coupled SST neurons also frequently showed AP-evoked spikelets onto paired neurons due to low-pass filtering (Fig. 8C_1; bottom panel, right), which results in a greater attenuation of the high frequency portion (spike), than the low frequency portion (AHP), of an action potential as it passes through an electrical synapse.

Of the 20 WT SST neuron pairs tested, 12 were coupled, and the majority (9/12) of those were one-way chemical connections (Fig. 8C_2). Of the 20 YH-HET SST neuron pairs tested, 17 were coupled, and the majority (13/17) of those were two-way, or bidirectionally, connected (Fig. 8C_2). Of the 3 bidirectionally connected WT SST neuron pairs, 2 were chemical and 1 was electrical, whereas of the 13 bidirectionally connected YH-HET SST neuron pairs, 7 were chemical and 6 were electrical (Fig. 8C_2).

Thus, these data suggest that heterozygous Y777H expression increases reciprocal connectivity among SST neurons, of both the chemical and electrical sort.

Finally, although we previously found no alterations in the sEPSC frequency onto the total population of YH-HOM GABAergic neurons, there was an increase in the sEPSC frequency onto those with an NFS phenotype (Shore et al., 2020), suggesting there may be a compensatory increase in excitatory drive onto NFS YH-HOM GABAergic neurons to offset the effects of their decreased membrane excitability. To assess whether there is a similar increase in sEPSC frequency onto SST-expressing YH-HET neurons, which showed a similar decrease in membrane excitability to that of NFS YH-HOM GABAergic neurons, we recorded sEPSCs onto voltage-clamped WT and YH-HET SST neurons. Indeed, there was an increase in sEPSC frequency onto YH-HET SST neurons compared with that of WT (Fig. 8D), suggesting a compensatory increase in excitatory drive onto the most impaired GABAergic subtype.

Acute cortical slice recordings confirm the reduced intrinsic excitability of YH-HET SST neurons.

Of the three GABAergic neuron populations assessed, SST-expressing neurons showed the strongest impairments, both direct and indirect, downstream of the heterozygous Y777H variant. Importantly, the observed effects on YH-HET SST neuron physiology were consistent with those that would be expected, based on YH-HET SST subthreshold K_{Na} current increases (Supplemental Fig. $5C_2$, and Fig. $5C_2$), and predicted, based on SST KCNT1 GOF neuron modeling data (Fig. $6F_1$ and $6F_2$). Thus, to test whether the most significant physiological alterations identified in cortical neuron cultures are also present in an experimental preparation with a more organized network, we crossed YH HET mice with homozygous GIN (GFP-expressing Inhibitory Neurons) mice, which express GFP in a subpopulation of SST-expressing neurons of the hippocampus and cortex (Ma et al., 2006; Oliva et al., 2000), and performed electrophysiological recordings in acute brain slices from WT and YH-HET progeny.

First, we assessed the effects of the heterozygous Y777H variant on the passive and active membrane properties by performing whole-cell, current-clamp recordings of layer 2/3, GFP-expressing neurons in motor and somatosensory cortical regions of slices prepared from P21–P30 mice (Fig. 9A). Incremental current injections to elicit APs demonstrated a strong impairment in AP generation downstream of the heterozygous Y777H variant, as the YH-HET GFP-expressing neurons fired fewer APs across all current steps than the WT GFP-expressing neurons, similar to that observed in the YH-HET SST cultured neurons. (Fig. 9B and 9C). Although YH-HET GFP-expressing neurons in slice did not show a significant decrease in input resistance relative to those from WT, they did show a large increase in rheobase current, without alterations in AP shape (Fig. 9D). Thus, we confirmed the main electrophysiological finding from culture—the reduced excitability of YH-HET SST neurons—in acute slices from YH-HET juvenile mice.

DISCUSSION

More than a decade ago, autosomal dominant mutations were identified in the sodium-gated potassium channel *KCNT1* in multiple patients with severe, childhood epilepsy syndromes (Barcia et al., 2012; Heron et al., 2012). *KCNT1*-related epilepsy patients suffer not only with frequent, early-onset seizures, but also with cognitive impairments, movement disorders, and sometimes additional behavioral and/or psychiatric problems (Bonardi et al., 2021). Unfortunately, after over 10 years of research efforts, *KCNT1*-related epilepsies remain highly refractory to current anti-seizure medications (Bonardi et al., 2021); thus, a better understanding of the pathological mechanisms underlying *KCNT1*-related epilepsies—from mutated gene to altered K^+ current to altered neuronal physiology to altered neural network to seizure—is imperative for advancing therapeutic strategies to improve seizure control and enhance patient quality of life.

Heterozygous vs. homozygous *KCNT1* GOF variant effects

Despite the heterozygous nature of *KCNT1* GOF variants in the overwhelming majority of *KCNT1*-related DEE patients, research efforts, including our own, have largely focused on homozygous GOF variant effects on channel function and neuronal physiology (Gertler et al., 2019; Kim et al., 2014; McTague et al., 2018; Mikati et al., 2015; Milligan et al., 2014; Quraishi et al., 2019; Shore et al., 2020; Tang et al., 2016). Heterozygous *KCNT1* GOF variant expression likely results in the formation of heteromeric KCNT1 channels, consisting of both WT and mutant subunits, whose characteristics and kinetics may differ from those of homomeric KCNT1 channels; thus, it is critical to distinguish between GOF variant effects in heteromeric and homomeric KCNT1 channels to identify the pathogenic mechanisms of *KCNT1* GOF variants in DEEs. Recent work in heterologous cells has shown that KCNT1 GOF heteromeric channels, with WT and mutant subunits, exhibit K_{Na} current increases that lie between those of WT and KCNT1 GOF homomeric channels (Cole et al., 2021; Dilena et al., 2018; Rizzo et al., 2016). Furthermore, other recent studies have similarly shown that heterozygous *Kcnt1* GOF variant expression in neurons causes effects on K_{Na} current and excitability that are intermediate to those of WT and homozygous variant-expressing neurons (Gertler et al., 2022; Wu et al., 2024).

Here, we assessed the effects of heterozygous expression of *Kcnt1*-Y777H on K_{Na} currents, neuronal physiology, and synaptic connectivity among cortical neuron subtypes in mice, and compared the effects to those observed previously with homozygous expression of the same variant (Shore et al., 2020). We found that the heterozygous YH variant caused similar effects on K_{Na} currents and neuronal physiology to those caused by the homozygous YH variant, including subthreshold-specific increases in K_{Na} current, altered AP shape, and impaired AP firing of NFS GABAergic neurons, but with magnitudes intermediate to those of WT and YH-HOM neurons. At the network and whole-animal level, we previously showed that homozygous expression of the YH variant in mice increases homotypic synaptic connectivity (E–E and I–I) and the E/I ratio, resulting in hypersynchronous, hyperexcitable YH-HOM

cortical networks and frequent seizures. Here, we found no evidence of similar network alterations in YH-HET cortical networks, which likely explains the infrequent seizures observed in the heterozygous YH mouse model, and together with the YH-HOM data, indicate a strong relationship between network abnormalities and seizure propensity downstream of the YH variant. Furthermore, these data suggest that heterozygous and homozygous *KCNT1* variant expression cause similar, gene-dose-dependent GOF effects at the current and neuron level, but not at the network or whole-animal level.

Neuron-type-dependent *KCNT1* GOF variant effects

Prior work has illustrated the importance of cell context in delineating the functional effects of ion channel variants on neuronal physiology. For instance, several studies using LOF channelopathy models of both sodium and potassium channels have identified excitability effects on one neuron type without effects on another (Hedrich et al., 2014; Soh et al., 2018; Tai et al., 2014; Yu et al., 2006). Other studies have shown that the same ion channel variant can even cause opposite effects on excitability in different neuron types (Makinson et al., 2016; Rush et al., 2006; Studtmann et al., 2022). Thus, understanding how KCNT GOF alters networks to lead to hyperexcitability and seizures requires a thorough evaluation of how the variant impacts each neuron type that participates in the network. With this goal in mind, we assessed the effects of heterozygous *Kcnt1* GOF on K_{Na} currents and AP generation among cortical glutamatergic neurons and all three major GABAergic neuron subtypes, including those expressing VIP, SST, and PV.

Using two methods to isolate and measure the KCNT1-mediated current, VU170- and TTX-subtraction, we observed voltage-dependent differences in current increases among the YH-HET neuron types. YH-HET glutamatergic and VIP neurons showed KCNT1-mediated current increases across suprathreshold voltages, whereas YH-HET SST and PV neurons had current increases across subthreshold voltages. These neuron-type dependent effects of KCNT1 GOF on K_{Na} current increases are

similar to those observed previously in YH-HOM, glutamatergic and GABAergic neuron subpopulations using TTX (Shore et al., 2020). Moreover, these results are similar to those reported in a recent study using a different KCNT1 GOF mouse model (human R474H, mouse R455H), which showed K_{Na} current increases selectively across positive potentials in glutamatergic, but across positive and negative potentials in FS and NFS GABAergic, neurons (Wu et al., 2024). The mechanism underlying these neuron-type-dependent KCNT1 GOF effects on K_{Na} current increases is unknown, however, we have observed differences even in WT KCNT1 channel activation curves between glutamatergic and VIP neurons (steeper slopes of activation) and SST and PV neurons (shallower slopes of activation), suggesting there are factors affecting KCNT1 channel kinetics that are inherent to each neuron type (Fig. 6A). Future studies should investigate these potential factors including (1) differential expression of alternative KCNT1 splice forms, some of which are known to have different activation kinetics, (2) differential expression of other channels such as KCNT2, which can form heteromers with KCNT1 and alter its biophysical properties, and (3) differential expression and/or localization of, and/or coupling to, sodium channels that act as the source of KCNT1 channel activation (Chen et al., 2009; Hage & Salkoff, 2012; Joiner et al., 1998).

Consistent with the differential KCNT1 GOF effects on K_{Na} currents, we observed a range of effects on membrane properties and AP generation among the cortical neuron populations. We observed no effects on YH-HET glutamatergic and VIP neurons, whereas YH-HET SST neurons showed reduced AP firing, with decreased input resistance and increased rheobase, and YH-HET PV neurons showed increased AP firing, with decreased rheobase. As a complementary approach, we performed *in silico* electrophysiology using our measured neuron-type-specific KCNT1 channel activation kinetics, with and without GOF, for each neuron type. For glutamatergic and VIP neurons, the steeper slopes of activation limited the effects of GOF on intrinsic excitability, whereas for SST neurons, the shallower slope of activation decreased the input resistance, increased the rheobase, and impaired AP generation

downstream of KCNT1 GOF. Each of these modeling results are similar to those observed using *in vitro* electrophysiology, indicating direct K_{Na} current-to-KCNT1 GOF phenotype relationships in these neuron types.

Conversely, for PV neurons, unlike the experimental observation of increased YH-HET PV neuron excitability, *in silico* electrophysiology predicted a slight reduction in PV neuron excitability downstream of KCNT1 GOF. In support of this *in silico* prediction, in a different KCNT1 GOF mouse model, heterozygous expression of the human L456F variant indeed reduced AP firing of PV neurons, without altering any other membrane properties or AP parameters (Gertler et al., 2022). The opposite effect of KCNT1 GOF on PV excitability between these two studies may simply result from variant-specific alterations in KCNT1 channel kinetics; however, both GOF variants showed a similar lack of effect on membrane properties and AP generation of glutamatergic neurons. Alternatively, the opposite effects could be due to the different experimental conditions used in the two studies, including (1) different preps and mouse ages (acute slices from P42–P60 mice vs. DIV 13–17 cultured neurons from P0 pups) and (2) different brain regions (hippocampal vs. cortical). The idea of brain region-dependent effects of ion channel variants is not unprecedented, as a recent study showed that a potassium channel GOF variant causes opposite effects on excitability in the same neuron type from different brain regions (hippocampal CA1 vs. cortical layer 2/3 pyramidal neurons), and this opposite effect was suggested to be due to the compensatory upregulation of sodium channels in one neuron type but not the other (Varghese et al., 2023). Taken together, these findings illustrate the importance of interrogating not only multiple neuron types but also multiple brain regions to fully unravel the complexity underlying KCNT1 GOF-related neurodevelopmental disorders.

Evidence of potential neuron and network compensatory responses to KCNT1 GOF

In a healthy brain, there are multiple homeostatic compensation mechanisms to maintain neuronal and network activity at their proper physiological levels (Davis, 2013; Debanne et al., 2019; Debanne & Russier, 2019; Marder & Goaillard, 2006; Turrigiano, 2011, 2012; Yang & Prescott, 2023), whereas in a brain with epilepsy-causing genetic mutations or injury, it is thought that failure of homeostatic compensation can result in hypersynchronous, hyperexcitable networks and, ultimately, seizures (Issa et al., 2023; Lignani et al., 2020; Staley, 2015). As YH-HET mice have only been observed to have infrequent seizures and YH-HET networks appear largely intact, it is plausible that there are adaptive or homeostatic mechanisms downstream of the YH variant that limit KCNT1 GOF effects largely to those observed at the current and neuron level. These regulatory mechanisms may include alterations in ion currents and/or synaptic input to restore proper AP shape or neuronal excitability, or alterations in chemical and/or electrical connectivity to stabilize neural networks.

Neuronal excitability is regulated by the inward and outward flow of opposing currents through sodium and potassium channels; thus, it is not surprising that mutations affecting these channels can lead to compensatory up- or down-regulation of other ion channels or currents to maintain excitability and proper neuron function. In this study, our *in silico* electrophysiology predictions of YH-HET PV neuron excitability were opposite to those of our *in vitro* electrophysiology data; thus, we hypothesized that there may be a compensatory increase in an ion current that counteracts the increased K_{Na} current selectively in YH-HET PV neurons. Accordingly, we identified a subthreshold increase in the persistent Na^+ current, across a similar voltage range to the increased K_{Na} current, in YH-HET PV, but not SST, neurons. Furthermore, *in silico* approaches indicated that this increased I_{NaP} was sufficient to overcome the effects of KCNT1 GOF and cause an overall increase in AP generation in YH-HET PV neurons, which aligned with our experimental data. Similar compensatory mechanisms have been identified in other models such as the downregulation of multiple potassium channels in a sodium channel (*Scn2a*) LOF mouse model of epilepsy, resulting in neuronal hyperexcitability (Zhang et al., 2021), or the upregulation

of Na^+ currents in response to increased potassium channel activity in a developing Xenopus neural circuit, resulting in restored intrinsic excitability and network stability (Pratt & Aizenman, 2007). Notably, another KCNT1 GOF model (*Kcnt1*-R455H) showed upregulation of a sodium channel ($Na_v1.6$), accompanied by an increase in transient and persistent sodium currents, in *Kcnt1*-R455H cortical neurons, but the effects of Nav1.6 upregulation were not investigated (Wu et al., 2024).

As the persistent sodium current has been shown to act as a source of cytoplasmic sodium ions for KCNT1 channel activation in some neuron types (Hage & Salkoff, 2012), one might expect that the compensatory increase in I_{NaP} in YH-HET PV neurons would further increase, rather than counteract, K_{Na} currents. Unfortunately, there is insufficient information on the relative locations of the I_{NaP} and KCNT1 channels, as well as the kinetics of sodium transfer to KCNT1 channels, among cortical neuron subtypes, and even less is known in the context of KCNT1 GOF neurons; thus, it is difficult to predict how alterations in one of these currents may affect the other. One plausible reason that increased I_{NaP} would not alter K_{Na} currents in YH-HET PV neurons is that the particular sodium channels that are responsible for the increased I_{NaP} are not located within close proximity to the KCNT1 channels. Moreover, homeostatic mechanisms that modify the length and/or location of the sodium channel-enriched axon initial segment (AIS) in neurons in response to altered excitability are well described (Grubb & Burrone, 2010; Kuba et al., 2010); thus, it is possible that in YH-HET PV neurons, the length or location of the AIS is altered, leading to uncoupling of the sodium channels that are responsible for the increased I_{NaP} to the KCNT1 channels. Future studies will aim to further investigate potential mechanisms of neuron-type-specific alterations in NaP and K_{Na} currents downstream of KCNT1 GOF.

In addition to the KCNT1 GOF current-mediated impairments in SST neuron excitability, we identified several potential compensatory YH-HET SST synaptic and network alterations. For instance, there was an increased frequency of sEPSCs onto YH-HET SST neurons, suggestive of a compensatory increase in excitatory input to counteract their reduced intrinsic excitability and increase their AP firing,

as has been observed previously in hypoexcitable SST neurons in another epilepsy model (Halabisky et al., 2010). There was also an increase in chemical and electrical coupling between YH-HET SST neurons. Although SST neurons normally show a relatively low rate of homotypic chemical coupling, particularly in the adult cortex, more than half of nearby SST neuron pairs are coupled electrically (Amitai et al., 2002; Gibson et al., 1999, 2005; Hu & Agmon, 2015; Urban-Ciecko & Barth, 2016). This coupling is thought to be important for fine tuning neural circuits by regulating such processes as synchronous AP firing, synaptic integration, and network rhythmicity (Alcami & Pereda, 2019; Connors, 2017). The observed increase in electrical coupling should not only contribute to the reduced intrinsic excitability properties of individual YH-HET SST neurons, increasing their capacitance and decreasing their input resistance, but may also act as a homeostatic mechanism to restore synchronicity and stability to YH-HET SST networks (Lane et al., 2016; Parker et al., 2009).

Taken together, how might the YH-HET variant-induced alterations to SST and PV neurons, both direct and adaptive, ultimately contribute to neural network behavior and seizure propensity in YH-HET mice? The paucity of effects on synaptic activity and connectivity in YH-HET networks, relative to those of YH-HOM, suggests that the current- and neuron-level effects of the YH-HET variant are below some threshold required to induce broader network hyperexcitability and seizures. Moreover, as described above, several of the proposed homeostatic mechanisms, such as increased excitatory input onto, and connectivity between, SST neurons and increased I_{NaP} in PV neurons, should theoretically act to suppress pathological network activity in YH HET mice. However, predicting the downstream effects of altered SST and PV intrinsic excitability is not straightforward, particularly with the emerging appreciation of both anti- and pro-epileptic roles for these neuron types in seizure initiation and maintenance (Dudok et al., 2022; Magloire et al., 2019). Furthermore, studies using genetic mouse models of DEEs have identified seemingly paradoxical, and sometimes ephemeral, roles of interneurons in disease progression. For instance, in an *SCN8A* GOF DEE mouse model, increased I_{NaP} causes initial SST

hyperexcitability followed by depolarization block, and in parallel, chemogenetic activation of WT SST neurons mimics these effects, leading to seizure generation (Wengert et al., 2021). Similarly, in a *KCNQ2/3* LOF DEE model, PV-specific *Kcnq2/3* deletion causes early PV hyperexcitability that is thought to increase seizure susceptibility via homeostatic potentiation of excitatory transmission (Soh et al., 2018). Lastly, in an *Scn1a*$^{+/-}$ mouse model of Dravet syndrome, PV neurons are transiently hypoexcitable during development, whereas later they show an increased firing rate, both interictally and at seizure onset, and a decrease in synchrony in the transition to seizure (Favero et al., 2018; Tran et al., 2020). These studies illustrate the challenges in connecting altered interneuron intrinsic excitability with network behavioral outcomes not only because of the contradictory nature of some of these connections but also because of the often transient nature of interneuron phenotypes during disease progression. Thus, future studies should aim to assess neuron-type-specific effects of the YH variant at different developmental time points in both YH-HET mice, with rare seizures, and YH-HOM mice, with frequent seizures, to better understand the contributions of interneuron dysfunction to network pathology and seizure generation in KCNT1 GOF-related epilepsy.

Limitations and Conclusions

The *in vitro* and *in silico* nature of this study are limitations. Although the cultured VIP, SST, and PV neurons showed characteristic electrophysiological properties, it is unknown how much overlap there is between the *in vitro* and *in vivo* populations. For instance, it is possible that our culture conditions select for more mature neurons of each type or preferentially support the survival of subpopulations; thus, we may be assessing KCNT1 GOF effects on a small portion of a given subtype. However, an advantage of the *in vitro* prep is that the compensatory alterations we observe are not likely consequences of seizure activity, which has been shown to alter interneuron properties in epilepsy models. Furthermore, the *in silico* neurons we used to model each neuron type were designed to

accurately reflect the morphological and electrophysiological properties of each subtype, but they may lack more detailed features of ion channels, such as post-translational modifications and subcellular localizations, that can have important functional effects. Our KCNT1 model conductance is also hampered by an incomplete understanding of the relationship between Na^+ influx, membrane voltage, and channel gating in neurons.

Moreover, our K^+ current measures using *Kcnt1*$^{-/-}$; *Kcnt2*$^{-/-}$ double knockout neurons clearly showed the presence of an outward VU170-sensitive current across positive potentials, indicating non-specific activity of this small molecule, potentially to the ERG K^+ channel (Spitznagel et al., 2020). This off-target effect of VU170 may contribute to the overall increase in outward K^+ currents seen in our VU170- vs TTX-subtracted currents in all neuron types across positive potentials, and it limits the interpretation of the VU170-sensitive K_{Na} current data within this range. Finally, although it is well known that temperature changes can alter neuron physiology, the electrophysiological recordings in this study were performed at room temperature rather than physiological temperature. In this study, we further assessed the effect of temperature (22°C vs. 35°C) on rheobase, AP amplitude, and maximal AP firing frequency among WT and YH-HET PV neurons and showed that both groups responded similarly. Previously, we also showed that the effects of the homozygous YH variant on glutamatergic and NFS GABAergic neuron excitability were highly similar between cultured recordings at room temperature (~22°C) and slice recordings at 32°C. Taken together, these data suggest that the reported neurophysiological phenotypes downstream of the YH variant are likely not temperature dependent.

Despite the potential limitations, this study provides three major findings that advance our understanding of the relationship between ion channel function and disease. First, heterozygous *KCNT1* expression causes changes in current flow and neuron excitability that are qualitatively similar to homozygous expression, but of a lower magnitude; however, the synaptic activity and connectivity changes are different, which likely leads to the discrepancy in seizure incidence. This finding suggests a

non-linear relationship between GOF, at the level of the ion channel current, and disease severity. Second, the same *KCNT1* variant can produce opposite effects on neuron excitability in closely related GABAergic neuron subtypes, and these opposite effects are likely due to compensation in one neuron type (PV) that is absent in the other (SST). Previous studies have observed opposite effects on neuronal excitability due to Na^+ channel variants, but the underlying mechanism, when explored, was proposed to be intrinsic differences in ion channel expression, not compensation. Third, we observed increased synaptic and gap junction connectivity among SST neurons, demonstrating that the effects of KCNT1 GOF extend to structural alterations as well. The effects of this increased connectivity, especially by gap junctions, on neuronal excitability and network behavior offers an exciting avenue for future research. Finally, it will be critical to determine whether these alterations downstream of KCNT1 GOF potentiate or attenuate network pathology and seizure activity, thus providing a better understanding of disease mechanisms and prompting novel therapeutic design.

MATERIALS AND METHODS

Mice

Mice were bred, and mouse procedures were conducted, in compliance with the National Institutes of Health (NIH) Guidelines for the Care and Use of Laboratory Animals and were approved by the Institutional Animal Care and Use Committee at the University of Vermont (animal protocol numbers: 16-001, 19-034, and X9-022). Mice were maintained in ventilated cages at controlled temperature (22–23°C), humidity ~60%, and 12-h light: 12-h dark cycles (lights on at 7:00 AM, off 7:00 PM). Mice had access to regular chow and water, *ad libitum*. For all experiments, male and female littermates were used for each genotype. The ages of the mice for each experiment are indicated in the following relevant sections.

Mouse lines and strains used for these studies include: *Kcnt1*^{Y777H} knockin in the C57BL/6NJ (B6NJ) strain (formal gene and allele symbol: *Kcnt1*$^{em1(Y777H)Frk}$), *Sst*-IRES-Cre (*Sst*$^{tm2.1(cre)Zjh}$/J; Jackson Labs stock: 013044), *Vip*-IRES-Cre (*Vip*$^{tm1(cre)Zjh}$/J; Jackson Labs stock: 010908), *Pvalb*-IRES-Cre (B6.129P2-*Pvalb*$^{tm1(cre)Arbr}$/J; Jackson Lab stock: 017320), C57Bl/6J (Jackson Labs stock: 000664), and GIN (FVB-Tg(GadGFP)45704Swn/J; Jackson Lab stock: 003718) mice.

Kcnt1^{Y777H} mice were genotyped using PCR amplification primers (*Kcnt1* forward primer: 5'-CTAGGGCTGCAAACACAACA-3'; *Kcnt1* reverse primer: 5'-TCAAGCAGCAACACGATAGG-3') with standard thermocycler amplification conditions, and the annealing temperature set at 58°C. Following amplification, a restriction cut was performed with the enzyme *Nla*III to distinguish mutant (127 and 44 bp products after cut) from wildtype (WT) alleles (171 bp product). Progeny of the *Kcnt1*^{Y777H} mice crossed to each Cre mouse line were genotyped for the presence of a *Cre* transgene using a forward primer (5'-TCGCGATTATCT TCTATA TCTTCAG-3') and reverse primer (5'-GCTCGACCAGTTTAGTTACCC-3'), resulting in a 455 bp product.

Primary Astrocyte Feeder Layer Culture

Astrocyte feeder layers were generated to support the growth and maintenance of primary neurons. Briefly, cortices were dissected from P0–P1 WT C57BL/6J mice (Jackson Labs stock: 000664) of either sex. The cortices were incubated in 0.05% trypsin-EDTA (Gibco) for 15 min at 37°C in a Thermomixer (Eppendorf) with gentle agitation (800 rpm). Then, the cortices were mechanically dissociated with a 1-mL pipette tip, and the cells were plated into T-75 flasks containing filter-sterilized astrocyte media [DMEM media supplemented with glutamine (Gibco), 10% fetal bovine serum (FBS, GE Healthcare), 1X MITO+ Serum Extender (Corning), and 0.2X penicillin/streptomycin (Gibco)]. After the astrocytes reached confluency, they were washed with PBS (Gibco) and incubated for 5 min in 0.05% trypsin-EDTA

at 37°C, washed, and then resuspended in astrocyte media. Astrocytes were added to 6-well plates containing 25-mm coverslips precoated with coating mixture [0.7 mg/ml collagen I (Corning) and 0.1 mg/ml poly-D-lysine (Sigma) in 10 mM acetic acid].

Primary Cortical Neuron Culture

For the primary neuron culture, the dorsomedial cortices from P0–P1 WT and *Kcnt1*$^{m/+}$ mice of both sexes were dissected in cold HBSS (Gibco). The tissue was then digested with papain (Worthington) for 60–75 min and treated with inactivating solution (Worthington) for 10 min, both while shaking at 800 rpm at 37°C in a Thermomixer. The cells were then mechanically dissociated and counted. The dissociated cells were added at 200,000 cells/well to 6-well plates containing astrocyte-coated coverslips in filter-sterilized NBA plus [Neurobasal-A medium (Gibco) supplemented with 1X Glutamax (Gibco), 1X B27 (Invitrogen), and 0.2X penicillin/streptomycin (Gibco)]. After plating (12-24 h), approximately 4×10^{10} genome copies (GC) of AAV8-*CaMKII*-GFP (UNC Vector Core) were added to each well. For experiments to assess KCNT1 effects on GABAergic subtypes, approximately 4×10^{10} genome copies (GC) of AAV9-*hSyn*-DIO-mCherry (addgene) were also added to each well to mark Cre-expressing neurons. Every 3–4 days, 20–40% of the media was replaced with fresh NBA plus.

Electrophysiology

Whole-cell recordings were performed with patch-clamp amplifiers (MultiClamp 700B; Molecular Devices) under the control of Clampex 10.3 or 10.5 (Molecular Devices, pClamp, RRID:SCR_011323). Data were acquired at 20 kHz and low-pass filtered at 6 kHz. The series resistance was compensated at 70%, and only cells with series resistances maintained at less than 15 MΩ were analyzed. Patch electrodes were pulled from 1.5-mm o.d. thin-walled glass capillaries (Sutter Instruments) in five stages on a micropipette puller (model P-97; Sutter Instruments). Internal solution contained the following: 136

mM K-gluconate, 17.8 mM HEPES, 1 mM EGTA, 0.6 mM $MgCl_2$, 4 mM ATP, 0.3 mM GTP, 12 mM creatine phosphate, and 50 U/ml phosphocreatine kinase. Alternatively, internal solution contained: 136 mm KCl, 17.8 mm HEPES, 1 mm EGTA, 0.6 mm MgCl2, 4 mm ATP, 0.3 mm GTP, 12 mm creatine phosphate, and 50 U/ml phosphocreatine kinase. The pipette resistance was between 2 and 4 MΩ. Standard extracellular solution contained the following (in mM): 140 NaCl, 2.4 KCl, 10 HEPES, 10 glucose, 4 $MgCl_2$, and 2 $CaCl_2$ (pH 7.3, 305 mOsm). All experiments were performed at room temperature (22–23°C), with the exception of the current-clamp experiments to compare the effects of temperature on neuronal physiology (Supplemental Figure 4-3). For these recordings, all current-clamp parameters were measured first at room temperature, then the temperature of the external solution was heated to 35°C using a ThermoClamp Inline Heater (ThermoClamp-3; AutoMate Scientific), and the measurements were repeated. Whole-cell recordings were performed on cortical neurons from control and mutant groups in parallel on the same day (day 13–17 *in vitro*). All experiments were performed by two independent investigators blinded to the genotypes.

For current-clamp experiments, the intrinsic electrophysiological properties of neurons were tested by injecting 500-ms square current pulses incrementing in 20 pA steps, starting at −100 pA. Resting membrane potential (V_m) was calculated from a 50 ms average before current injection. The membrane time constant (τ) was calculated from an exponential fit of current stimulus offset. Input resistance (R_{in}) was calculated from the steady state of the voltage responses to the hyperpolarizing current steps. Membrane capacitance was calculated by dividing the time constant by the input resistance. Action potentials (APs) were evoked with 0.5 s, 20 pA depolarizing current steps. Rheobase was defined as the minimum current required to evoke an AP during the 500 ms of sustained somatic current injections. AP threshold was defined as the membrane potential at the inflection point of the rising phase of the AP. AP amplitude was defined as the difference in membrane potential between the AP peak and threshold,

and the afterhyperpolarization (AHP) was the difference between the AP threshold and the lowest V_m value within 50 ms. The AP half-width was defined as the width of the AP at half-maximal amplitude. To obtain the neuron's maximum firing frequency, depolarizing currents in 20-pA steps were injected until the number of APs per stimulus reached a plateau phase. The membrane potential values were not corrected for the liquid junction potential. GABAergic neurons were classified as fast spiking (FS) if their maximum mean firing rate reached above 60 Hz and their AP half-widths increased by less than 25% during 1 s of sustained firing (Avermann et al., 2012; Casale et al., 2015). All others were considered non-fast spiking (NFS).

For voltage-clamp experiments to measure synaptic currents, neurons were held at -70 mV, except for evoked IPSC measurements, for which neurons were held at 0 mV. AP-evoked EPSCs were triggered by a 2 ms somatic depolarization to 0 mV. The shape of the evoked response, the reversal potential and the effect of receptor antagonists [10 µM NBQX (Tocris Bioscience) or 20 µM bicuculline (BIC, Tocris Bioscience)] were analyzed to verify the glutamatergic or GABAergic identities of the currents. Neurons were stimulated at 0.1 Hz in standard external solution to measure basal-evoked synaptic responses. Electrophysiology data were analyzed offline with AxoGraph X software (AxoGraph Scientific, RRID:SCR_014284). Spontaneous synaptic potentials were recorded in control solution with either NBQX or bicuculline to isolate EPSCs or IPSCs, respectively. Data were filtered at 1 kHz and analyzed using template-based miniature event detection algorithms implemented in the AxoGraph X. The threshold for detection was set at three times the baseline SD from a template of 0.5 ms rise time and 3 ms decay. The E/I ratio was calculated as the product of the sEPSC frequency and charge over the sum of the sEPSC frequency and charge and the product of the sIPSC frequency and charge.

K_{Na} and KCNT1 Current Measurements

For voltage-clamp experiments to measure the sodium-activated K^+ current or KCNT1-mediated current, neurons were held at -70 mV and given 1 s voltage pulses in 10 mV steps over a range of -80 to +50 mV. Recordings were obtained for each cell in standard extracellular solution or extracellular solution containing 0.5 µM tetrodotoxin (TTX) or 10 µM VU170. TTX or VU170 was applied directly on the recorded neuron with a custom-built fast flow perfusion system capable of complete solution exchange in less than 1 s to minimize the time interval between control and drug recordings and current rundown. Current traces from the TTX or VU170 solution were subtracted from the current traces obtained from the standard solution. The difference current over the 100 ms at the end of the voltage pulse was considered the steady state K_{Na} current. The same protocol was used for outside-out patch experiments.

I_{NaP} Current Measurements

For voltage-clamp experiments to measure the persistent Na^+ current, neurons were held at -80 mV and given a 5 s voltage ramp at 20 mV/s. The ramp was repeated every 10 s. Recordings were obtained for each cell in standard extracellular solution or extracellular solution containing 0.5 µM TTX. TTX was applied directly on the recorded neuron with a custom-built fast flow perfusion system capable of complete solution exchange in less than 1 s to minimize the time interval between control and TTX recordings. The first current trace after TTX application was subtracted from the averaged current traces obtained from the standard solution. At this time point, the effect of TTX on the Na^+-activated K^+ current is minimal, while the persistent Na^+ current is maximally inhibited. This allowed us to isolate the persistent Na^+ current from K_{Na} and obtain a more accurate estimate of changes in I_{NaP}.

Neuron Modeling

Model neurons (~10 per class) representing excitatory (Pyramidal Cell, PC), SST (Martinotti Cell, MC), PV (Large Basket Cell, LBC), and (Bipolar Cell, BP) VIP neurons were downloaded from the EPFL/Blue Brain

project (https://bbp.epfl.ch/nmc-portal/downloads.html), and implemented in the NEURON environment. Because no KCNT1-like conductance was present in the original models, a Hodgkin-Huxley KCNT1 model conductance was created with both Na^+- and voltage-dependent gates and inserted into the dendritic, somatic, and axonal compartments of model neurons (0.03 S/cm^2). The Na^+ dependence was modeled after Bischoff et al. (EC_{50} = 40 mM, slope 3.5), and the voltage dependence was modeled after our own experimental data (Fig. 5), corrected to account for the calculated liquid junction potential in the experimental data. To verify that this approach reproduced experimental data, voltage step protocols were run in NEURON with 10 mM and 0 mM internal Na^+. "K_{Na}" currents were obtained by subtraction, and the amplitude and kinetics of the resulting currents were verified to be similar to experimental values. To model the effects of KCNT1 GOF, the EC_{50} for Na^+ was decreased to either 35 or 30 mM, because the Y796H variant was previously shown to increase the Na^+ sensitivity of the channel. These changes resulted in moderate increases in the current above WT levels (Fig. 6B), consistent with the experimental data (Fig. 4 and Fig. 5). Modeling data was generated by running current clamp protocols in NEURON for each of the model neurons and analyzed in the same way as experimental data. For modeling the increase in I_{NaP}, the control I_{NaP} conductance was set to 0.001 times the conductance of the transient Na^+ current in each compartment. This produced I_{NaP} currents approximately 1% of the peak of the transient Na^+ current. KCNT1 GOF was modeled by decreasing the Na^+ EC_{50} to 30 mM and the I_{NaP} increase was modeled by increasing its conductance 2-fold, in accordance with experimental data.

Immunostaining, Imaging, and Quantification

For live imaging of GABAergic subtypes *in vitro*, cortical neurons isolated and cultured from VIP-Cre, SST-Cre, and PV-Cre pups, were infected with AAV-*CamKII*-GFP and AAV-*hSyn*-DIO-mCherry viruses at DIV 1 to mark glutamatergic and Cre-expressing, GABAergic neurons, respectively. Images were captured from

live cultures at DIV 14 (VIP-Cre and SST-Cre) or DIV 16 (PV-Cre) using an inverted Olympus IX73 epifluorescent microscope with an Olympus PlanFluor 10× objective lens and an Andor Zyla sCMOS 4.2 camera controlled by µManager 2.0-β software (Edelstein et al., 2014). The same acquisition parameters were used for each image and each group.

For soma size measurements, DIV 16 cultured SST-Cre neurons on coverslips were washed three times with prewarmed PBS, fixed with 4% paraformaldehyde in PBS for 30 min at room temperature, and then washed again three times with PBS. The fixed neurons were then incubated in blocking buffer (10% normal goat serum and 0.1% Triton-100 in 1X PBS) for 1 h at room temperature, followed by incubation with a Neu-N primary antibody (Synaptic Systems 266-004) diluted in blocking buffer (1:500) overnight at 4°C. The next day, the neurons were washed three times with PBS for 10–15 min, incubated with goat anti-guinea pig, Alexa Fluor 647 secondary antibody (Invitrogen A21450) in blocking buffer (1:1000) for 1 h at room temperature, and washed again three times with PBS for 10–15 min. The coverslips were then flipped and mounted on glass slides using Fluoromount G with DAPI. Images (1024 × 1024 pixels) of Neu-N to mark all neurons, *CamKII*-GFP to mark glutamatergic neurons, and *hSyn*-DIO-mCherry to mark Cre-expressing neurons, were obtained using a DeltaVision Restoration Microscopy System (Applied Precision/GE Life Sciences) with an inverted Olympus IX70 microscope with a 20 × oil objective, SoftWoRx software, and a CoolSNAP-HQ charge-coupled device digital camera (Photometrics). Image exposure times and settings were kept the same between groups in a culture and were optimized to ensure that there were no saturated pixels. To analyze soma size, regions of interest (ROIs) were drawn around cell bodies using the mCherry channel with Fiji software (Schindelin et al., 2012), and then the cell body areas were measured for each mCherry^{+} neuron imaged.

Mouse cortex slice preparation

Cortical slices were prepared from P21–P30 WT and *Kcnt1*-Y777H heterozygous pups, which were the progeny of *Kcnt1*-Y777H heterozygous mice crossed to homozygous GIN mice (JAX stock #003718), which express GFP in a subset of SST-positive neurons (Ma et al., 2006; Oliva et al., 2000), following a modified protocol (Ting et al., 2014). Briefly, mice were deeply anesthetized with isoflurane and transcardially perfused with 25–30 mL of ice-cold NMDG aCSF (in mM: 93 NMDG, 2.5 KCl, 1.2 NaH_2PO_4, 30 $NaHCO_3$, 20 HEPES, 25 D-glucose, 5 Na-ascorbate, 2 thiourea, 3 Na-pyruvate, 12 N-acetyl-L-cysteine, 10 $MgSO_4$, 0.5 $CaCl_2$, with pH adjusted to 7.3–7.4 with 10 N HCl) that was saturated with carbogen (95% O_2, 5% CO_2 (pH 7.3–7.4). The mice were rapidly decapitated, and the heads were submerged in ice-cold NMDG aCSF bubbled with carbogen. After extraction from the skull, the cortex was blocked and 250-µm coronal sections were cut with a vibrating microslicer (Leica VT100S, Leica Biosystems) while submerged in the same solution. Slices were first moved to NMDG aCSF at 32–34°C for a short-term recovery (≤ 15 min) before being transferred into HEPES-based holding aCSF (in mM: 92 NaCl, 2.5 KCl, 1.2 NaH_2PO_4, 30 $NaHCO_3$, 20 HEPES, 25 D-glucose, 5 Na-ascorbate, 2 thiourea, 3 Na-pyruvate, 12 N-acetyl-L-cysteine, 2 $MgSO_4$, 2 $CaCl_2$, bubbled with carbogen, with pH adjusted to 7.3–7.4 with KOH or HCl as necessary). The slices were held in this solution until use.

Ex vivo slice electrophysiology

For recording, the cortical slices were placed in a chamber mounted on a fluorescence microscope (Zeiss Axio Examiner.D1) and perfused with normal Ringer's solution containing (in mM): 130 NaCl, 3 KCl, 2 $MgCl_2$, 2 $CaCl_2$, 1.25 NaH_2PO_4, 26 $NaHCO_3$, and 10 D-glucose, bubbled with carbogen. Patch electrodes were pulled from 1.5-mm o.d. thin-walled glass capillaries (Garner Glass Company) in two stages on a micropipette puller (model P-1000; Sutter Instruments). Electrophysiological recordings were obtained from GFP-labeled neurons in layer 2/3 of either motor or somatosensory cortex using pClamp, an MultiClamp 700B amplifier, and a Digidata 1440A analog-to-digital converter (Molecular Devices). Data

were acquired at 20 kHz and low-pass filtered at 10 kHz. Internal solution contained the following (in mM): 17.5 KCl, 112.5 K-gluconate, 1.5 NaCl, 5 Na_2-phosphocreatine, 1 $MgCl_2$, 10 HEPES, 0.2 EGTA, 3 Mg-ATP, 0.3 GTP-Tris (pH 7.2, with KOH). The pipette resistance was between 3 and 5 MΩ. All experiments were performed at room temperature (22–23°C).

The intrinsic electrophysiological properties of neurons were tested using current-clamp recording under whole-cell configuration by injecting 1 s square current pulses in 5-pA steps, starting at −30 pA. All recordings were saved in the computer for off-line analysis using Clampfit 11.2 or Axograph X software. The membrane time constant (τ) was calculated from an exponential fit of current stimulus offset. Input resistance (R_{in}) was calculated from the steady state of the voltage responses to the hyperpolarizing current steps. Membrane capacitance was calculated by dividing the time constant by the input resistance. Action potential (AP) frequency was counted on each depolarizing current step and plotted as a function of injection current. Rheobase was defined as the minimum current required to evoke an AP during the 1 s of sustained somatic current injections. AP threshold was defined as the membrane potential at the inflection point of the rising phase of the AP, and the afterhyperpolarization (AHP) was the difference between the AP threshold and the lowest V_m value within 50 ms. The membrane potential values were not corrected for the liquid junction potential.

Data Presentation and Statistical Analysis

Prism 10 (GraphPad Prism, RRID:SCR_002798) was used to create all graphs. To test for statistical significance for all whole cell electrophysiology experiments, we used generalized linear mixed models (GLMM) in SPSS [28.0 Chicago, Ill (IBM, RRID:SCR_002865], which allows for within-subject correlations and the specification of the most appropriate distribution for the data. Because neurons and animals from the same culture or animal are not independent measurements, culture or litter was used as the

subject variable, and animals, neurons, and voltage steps were considered within-subject measurements. All data distributions were assessed with the Shapiro-Wilk test. Datasets that were significantly different from the normal distribution ($p < 0.05$) were fit with models using the gamma distribution and a log link function, except for synaptic connection probability, which was fit with the binomial distribution and probit link. Normal datasets were fit with models using a linear distribution and identity link. We used the model-based estimator for the covariance matrix and goodness of fit was determined using the corrected quasi likelihood under independence model criterion and by the visual assessment of residuals. All values reported in the text, figures, and tables are estimated marginal means +/- standard error, except where noted.

Acknowledgements

This work was supported by NIH/NINDS grants NS087095 (M.C.W.), NS110945 (M.C.W.), NS031348 (W.N.F.), R33NS109521 (C.D.W. and K.A.E.), and OD020351 (The Jackson Laboratory Center for Precision Genetics). The authors would like to acknowledge the support of the Microscopy Imaging Center (RRID# SCR_018821) and the Cellular & Molecular Core at the University of Vermont.

Author Contributions: Conceptualization, A.N.S., W.N.F., M.C.W.; Methodology, A.M.Q., B.D.S., K.A.E., C.D.W., Formal Analysis, A.N.S., M.C.W. K.L., M.S.; Investigation, A.N.S., M.C.W., K.L., M.S.; Writing-Original Draft, A.N.S, M.C.W., Revising and Editing, A.N.S., M.C.W.; Supervision, K.A.E., C.D.W., W.N.F., M.C.W.; Funding Acquisition, W.N.F., M.C.W.

FIGURE LEGENDS

Figure 1. Heterozygous *Kcnt1*-Y777H expression alters AP shape and generation in NFS GABAergic neurons. (A_1-A_3) On the left, representative responses to step currents are shown for glutamatergic, and

FS and NFS GABAergic, WT (black) and YH-HET (colors) neurons (top to bottom), illustrating the input resistance (in response to a depolarizing step) and the rheobase (the first trace with an AP in response to a hyperpolarizing step) for each neuron type. On the right, bar graphs show quantification and mean ± SEM of the membrane properties and AP parameters for each neuron type for WT (grey) and YH-HET (colors) groups, with individual neuron measurements overlaid in scatter plots. The p-values are shown on each graph where $p < 0.05$. **(B_1-B_3)** Representative traces are shown at low, medium, and high current steps for glutamatergic, and FS and NFS GABAergic, WT (black) and YH-HET (colors) neurons (left to right). The line graphs below show the number of APs (mean ± SEM) per current injection step in WT (black) and YH-HET (colors) neurons. Statistical significance was tested using Generalized Linear Mixed Models, and p-values are shown on each graph where $p < 0.05$.

Figure 2. Heterozygous *Kcnt1*-Y777H expression increases subthreshold K_{Na} currents in NFS GABAergic neurons. (A_1-A_3) Representative traces in control (top), 0.5 µM TTX (middle), and the difference current (bottom) calculated by subtracting the membrane current response to voltage steps (-80 to +50 mV) from a holding potential of -70 mV in TTX from the response in control external solution in glutamatergic, and FS and NFS GABAergic, WT (black) and YH-HET (colors) neurons. To include all of the representative traces in the figures, and prevent overlap of the traces, the large inward sodium currents were removed from each set of traces using the masking tool in Adobe Illustrator. **(B_1-B_3)** Summary data shows the K_{Na} current (mean ± SEM) for each voltage step in glutamatergic, and FS and NFS GABAergic, WT (black and gray) and YH-HET (colors) neurons. The p-values are shown on each graph where $p < 0.05$, and the n values are the number of neurons recorded for each group. **(C_1-C_3)** Plots of the K_{Na} current (mean ± SEM) for each voltage step from -80 to 0 mV in WT (black and gray) and YH-HET (colors) neurons to illustrate the values that are too small to be seen on the graphs in B_1-B_3. The shaded red area in C_3 indicates the subthreshold voltage range with significantly higher K_{Na} currents (red voltages along x-axis indicate steps

where $p < 0.05$) in YH-HET relative to WT neurons. The p-values are shown on each graph where $p < 0.05$, and the n values are the number of neurons recorded for each group. Statistical significance for I-V plots was tested using Generalized Linear Mixed Models with genotype and voltage step as fixed effects followed by pairwise comparisons at each level.

Figure 3. Heterozygous *Kcnt1*-Y777H expression does not alter synaptic connectivity or the excitation-inhibition balance. (A_1-A_4) Evoked postsynaptic currents (PSCs) were recorded from neuron pairs [glutamatergic (excitatory, E) and GABAergic (inhibitory, I)] by stimulating the neuron type indicated on the left and recording the response in the neuron type indicated on the right (WT, gray; YH-HET E, green; YH-HET I, red). Bar graphs below each recorded neuron pair schematic show summary data (mean ± SEM) of the connection probability (left graph; numbers on bars represent connected pair number/recorded pair number) and peak evoked PSC amplitude (right graph; dots represent individual evoked responses) between each motif. **(B_1)** Bar graphs with overlaid individual neuron measurements and mean ± SEM show the spontaneous EPSC (sEPSC) or IPSC (sIPSC) frequency onto E neurons (WT, gray; YH-HET, green). **(B_2)** Bar graphs with overlaid individual neuron measurements and mean ± SEM show the sEPSC or sIPSC frequency onto I neurons (WT, gray; YH-HET, red). **(B_3)** Scatter plots show individual E/I ratio measurements onto E neurons (WT, gray; YH-HET, green) and I neurons (WT, gray; YH-HET, red). The p-values are shown on each graph where $p < 0.05$.

Figure 4. Heterozygous *Kcnt1*-Y777H expression differentially affects the intrinsic excitability of SST- and PV-expressing GABAergic neurons. (A) A schematic diagram illustrates the strategy for generating fluorescently labeled GABAergic subtype-specific neurons. YH-HET mice were crossed to VIP-, SST-, or PV-Cre mice, and the resulting P0 WT and YH-HET littermate pups were used to isolate and culture cortical neurons. At DIV 1, neurons were infected with AAV-*CamKII*-GFP to label glutamatergic neurons,

and AAV-*hSyn*-DIO-mCherry to label Cre-expressing neurons. At DIV 13–17, whole-cell, patch-clamp electrophysiology was performed on mCherry$^+$/GFP$^-$ neurons. **(B_1-B_3)** On the left, representative responses to step currents are shown for VIP-, SST-, and PV-expressing WT (black) and YH-HET (colors) neurons (top to bottom). For each neuron type, the superimposed dark traces illustrate the input resistance (in response to a depolarizing step) and the rheobase (the first trace with an AP in response to a hyperpolarizing step), and the light trace shows the first step current response to induce repetitive AP firing across the step. Above the superimposed traces, the first AP of each rheobase trace is shown (same vertical scale, increased horizontal scale). On the right, bar graphs show quantification of the membrane properties and AP parameters for each neuron type (VIP, SST, and PV, top to bottom) for WT (grey) and YH-HET (colors) groups, with individual neuron measurements overlaid in scatter plots. The p-values are shown above each graph where $p < 0.05$. **(C_1-C_3)** For VIP-, SST-, and PV-expressing neurons (left to right), representative traces are shown at low, medium, and high current steps, and the line graphs below show the number of APs (mean ± SEM) per current injection step in WT (black) and YH-HET (colors) neurons. Statistical significance was tested using Generalized Linear Mixed Models, and p-values are shown above each graph where $p < 0.05$.

Figure 5. The *Kcnt1*-Y777H variant increases KCNT1-mediated currents across subthreshold voltages in SST- and PV-expressing GABAergic neurons. (A_1-A_3) Representative traces in control (top), 10 µM VU170 (middle), and the difference current (bottom) calculated by subtracting the membrane current response to voltage steps (-80 to +50 mV) from a holding potential of -70 mV in VU170 from the response in control external solution in VIP-, SST-, and PV-expressing, WT (black) and YH-HET (colors) neurons. To include all of the representative traces in the figures, and prevent overlap of the traces, the large inward sodium currents were removed from each set of traces using the masking tool in Adobe Illustrator. **(B_1-B_3)** Summary data shows the KCNT1 current (mean ± SEM) for each voltage step in VIP-,

SST-, and PV-expressing, WT (black and gray) and YH-HET (colors) neurons. The p-values are shown on each graph where $p < 0.05$, and the n values are the number of neurons recorded for each group. **(C_1-C_3)** Plots of the K_{Na} current (mean ± SEM) for each voltage step from -80 to 0 mV in WT (black and gray) and YH-HET (colors) neurons to illustrate the values that are too small to be seen on the graphs in B_1-B_3. The shaded red areas in C_2 and C_3 indicate the subthreshold voltage range with significantly higher K_{Na} currents ($p < 0.05$) in YH-HET relative to WT neurons. Statistical significance for I-V plots was tested using Generalized Linear Mixed Models with genotype and voltage step as fixed effects followed by pairwise comparisons at each level.

Figure 6. Compartmental models of KCNT1 GOF in SST, but not PV, neurons are consistent with experimental data. (A) Activation curves for VIP, SST, and PV neurons used to model the KCNT1 channel in each neuron type. **(B)** Representative traces of the response of an outside-out membrane patch pulled from an SST neuron in control external solution (top) and after application of 10 µm VU170 (bottom). **(C)** Representative trace of the VU170-sensitive current in an outside-out patch pulled from an SST neuron with a single exponential fit (red curve) overlaid and summary data showing the time constant (mean ± SEM) obtained from these fits. **(D)** Simulated traces showing the KCNT1-mediated current in model neurons at three levels of Na^+-sensitivity (Con-40 mM, GOF-35 mM, and GOF-30 mM). **(E_1, F_1, and G_1)** Simulated traces from model VIP (E_1; purple), SST (F_1; blue), and PV (G_1; yellow) neurons in response to 500-ms current injections at three levels of Na^+-sensitivity [control (Con), and two levels of KCNT1 GOF]. Representative traces are shown at increasing current steps from bottom to top for each level. **(E_2, F_2, and G_2)** Summary data from 10 model VIP (E_2; purple), SST (F_2; blue), and PV (G_2; yellow) neurons showing (from left to right) the number of APs at different current steps (F-I plot), the input resistance, and rheobase. The bar graphs (mean ± SEM) are overlaid with scatter plots of individual

neuron measurements. Statistical significance was tested using a Repeated Measures ANOVA. Asterisks indicate where $p < 0.05$ (*), $p \leq 0.01$ (**), and $p \leq 0.001$ (***).

Figure 7. The persistent Na^+ current is increased by the *Kcnt1*-Y777H variant in PV, but not SST, neurons. (A) Representative traces of WT (left) and YH-HET (right) SST neurons in response to slow voltage ramp in control (dark gray) and 7 seconds after application of 0.5 nM TTX (light gray) with the difference current (I_{NaP}) plotted on the same scale. **(B)** I_{NaP} I-V curves of WT (gray) and YH-HET (blue) SST neurons constructed from averaging the ramp-evoked difference current (mean ± SEM) at 5-mV intervals (left), and a bar graph with overlaid scatter plot showing the peak negative value for each neuron (right). **(C)** Representative traces of WT (left) and YH-HET (right) PV neurons in response to slow voltage ramp in control (dark gray) and 7 seconds after application of 0.5 nM TTX (light gray) with the difference current (I_{NaP}) plotted on the same scale. The upper traces and difference currents are plotted on different scales. **(D)** I_{NaP} I-V curves of WT (gray) and YH-HET (orange) PV neurons constructed from averaging the ramp-evoked difference current (mean ± SEM) at 5-mV intervals (left), and a bar graph with overlaid scatter plot showing the peak negative value for each neuron (right). **(E)** Simulated traces from a model PV neuron in response to 500-ms current injections with control levels of KCNT1 (black traces) and KCNT1 GOF (Na^+ EC_{50} = 35 mM) with a 2-fold increase in I_{NaP} (orange traces). Representative traces are shown at increasing current steps from bottom to top for each level. **(F)** F-I plot shows the increase in AP firing (left), and a bar graph with overlaid scatter plot of individual neuron values shows the decrease in rheobase associated with modeling KCNT1 GOF (Na^+ EC_{50} = 35 mM) together with the increase in I_{NaP}. For modeling data, statistical significance was tested using a Repeated Measures ANOVA. Asterisks indicate where $p < 0.05$ (*), $p \leq 0.01$ (**), and $p \leq 0.001$ (***).

Figure 8. YH-HET SST neurons show increased chemical and electrical coupling and receive increased excitatory input. (A and B) Evoked postsynaptic currents (PSCs) were recorded from SST neuron pairs by stimulating each neuron at 0.1 Hz and recording the response onto the partner. **(A)** A bar graph shows the connection probability (mean + SEM) between SST neurons (WT, gray; YH-HET, blue; numbers on bars represent connected pair number/recorded pair number). **(B)** On the left, example traces of evoked IPSCs [individual IPSCs (light) overlaid by averaged IPSCs (dark)], and on the right, a graph of connection strength between SST neurons (WT, gray; YH-HET, blue; individual measurements and summary violin plots). **(C_1)** A schematic illustrates representative responses (presynaptic, black; postsynaptic, red) between chemically coupled (upper two panels) and electrically coupled (lower two panels) SST neurons following 100-pA (left two panels) and AP (right two panels) stimulation. **(C_2)** Summary data of four possible connection motifs (not coupled, chemical: one-way, chemical: two-way, and electrical) tested among WT (gray box) and YH-HET (blue box) SST neuron pairs (20 pairs/group). **(D)** On the left, example traces of spontaneous EPSCs (sEPSCs) recorded onto SST neurons (WT, black; YH-HET, blue). On the right, a graph shows individual neuron measurements and summary violin plots of the sEPSC frequency onto SST neurons (WT, gray; YH-HET, blue). All significant p-values are displayed at the top of each graph.

Figure 9. Acute cortical slice recordings confirm the reduced intrinsic excitability of YH-HET SST neurons. (A) An inverted monochrome image illustrates the recording scheme from GFP-expressing neurons in acute slices from P21–P30 GIN mice that express GFP in a subset of SST-positive neurons. **(B)** Representative responses to current steps are shown for WT (black) and YH-HET (blue) to three, equivalent 1 s current steps. **(C)** Plot of the action potential frequency (mean ± SEM) per current injection step shows that YH-HET GFP-expressing neurons (blue) fire fewer action potentials than those of WT (grey) across a range of current inputs. **(D)** Bar graphs show quantification of the membrane

properties and AP parameters for WT (grey) and YH-HET (colors) GFP-expressing neuron groups, with individual neuron measurements overlaid in scatter plots.

Supplemental Figure 2-1. The magnitudes of the K_{Na} current increases in YH-HET glutamatergic and NFS GABAergic neurons are intermediate to those of WT and YH-HOM neurons. Bar graphs (top three) illustrate differences in K_{Na} current (mean ± SEM) between YH-HET [dark color; WT littermates (black)] and YH-HOM [light color; WT littermates (gray)] neurons for voltage steps where significant increases were previously observed (red asterisks where $p < 0.05$) in glutamatergic, and FS and NFS GABAergic, YH-HOM neurons. Line graphs (bottom three) illustrate differences in K_{Na} current (mean ± SEM) between YH-HET [dark color; WT littermates (black)] and YH-HOM [light color; WT littermates (gray)] neurons across negative voltage steps (-80 to -20 mV; red asterisks where $p < 0.05$ in YH-HOM compared with WT) in glutamatergic, and FS and NFS GABAergic, neurons.

Supplemental Figure 4-1. Cre recombinase-expressing, cortical GABAergic neuron subpopulations retain characteristic electrophysiological features in culture. Cortical neurons isolated and cultured from P0 pups (*Kcnt1*$^{+/+}$) from VIP-, SST-, or PV-Cre mouse lines were infected with AAV-*CamKII*-GFP to label glutamatergic neurons, and AAV-*hSyn*-DIO-mCherry to label Cre-expressing neurons, at DIV 1. **(A)** Images show GFP^{+} glutamatergic neurons and mCherry^{+} VIP-, SST-, or PV-expressing neurons (left to right) at DIV 14 (VIP and SST) or DIV 16 (PV). The scale bars represent 50 µm. **(B)** Representative responses to step currents are shown for VIP (purple), SST (blue), and PV (orange) neurons (left to right). For each neuron type, the superimposed dark traces illustrate the input resistance (in response to a depolarizing step) and the rheobase (the first trace with an AP in response to a hyperpolarizing step), and the light trace shows the first step current response to induce repetitive AP firing across the step. **(C)** On the left, the first AP of each rheobase trace is shown for VIP (purple), SST (blue), and PV (orange)

neurons. On the right, bar graphs show quantification of the membrane properties and AP parameters for each neuron type (VIP, SST, and PV, left to right), with individual neuron measurements overlaid in scatter plots.

Supplemental Figure 4-2. YH-HET SST neurons have increased soma size compared with those of WT. Cortical neurons were isolated and cultured from P0 pup progeny (WT and YH-HET) of YH-HET mice crossed to SST-Cre mice. Neurons were infected with AAV-*CamKII*-GFP to label glutamatergic neurons, and AAV-*hSyn*-DIO-mCherry to label Cre-expressing neurons, at DIV 1, and immunostained using anti-Neu-N antibodies at DIV 16. **(A)** Top two images show mCherry$^+$ SST-expressing neurons as a subpopulation of Neu-N$^+$ cortical neurons, and bottom two images show GFP$^-$, mCherry$^+$ SST-expressing neurons intermingled with GFP$^+$ glutamatergic neurons. The scale bars represent 50 µm. **(B)** A graph shows individual neuron measurements and summary violin plots of the mCherry$^+$ neuron soma size (WT, gray; YH-HET, blue) with the p-value displayed at the top.

Supplemental Figure 4-3. YH-HET and WT PV neurons show similar neurophysiological responses to increased temperature. YH-HET mice were crossed to PV-Cre mice, and the resulting P0 WT and YH-HET littermate pups were used to isolate and culture cortical neurons. At DIV 1, neurons were infected with AAV-*CamKII*-GFP to label glutamatergic neurons, and AAV-*hSyn*-DIO-mCherry to label Cre-expressing neurons. At DIV 16 and 17, whole-cell, patch-clamp electrophysiology was performed on glutamatergic (mCherry$^-$/GFP$^+$), GABAergic (mCherry$^-$/GFP$^-$), or PV (mCherry$^+$/GFP$^-$) neurons at room temperature (~22°C). Then, the external solution was warmed to 35°C, and the measurements were repeated. **(A)** Before-after plots of glutamatergic and GABAergic WT neurons (n=16) show alterations in all parameters measured with increased temperature, excluding the resting membrane potential (V_{rest}) and membrane capacitance (C_m). **(B)** Before-after plots show highly similar responses to temperature increases between

WT (n=11) and YH-HET (n=10) PV neurons for rheobase, AP amp, and maximal firing frequency (MFR). Empty circles represent individual neurons, and filled-in circles represent the averages for each group. Lines connect the before and after measurements for each neuron.

Supplemental Figure 5-1. The *Kcnt1*-Y777H variant increases K_{Na} currents measured with TTX subtraction across subthreshold voltages in SST-expressing GABAergic neurons. (A_1-A_3) Representative traces in control (top), 0.5 µM TTX (middle), and the difference current (bottom) calculated by subtracting the membrane current response to voltage steps (-80 to +50 mV) from a holding potential of -70 mV in TTX from the response in control external solution in VIP-, SST-, and PV-expressing, WT (black) and YH-HET (colors) neurons. To include all of the representative traces in the figures, and prevent overlap of the traces, the large transient inward sodium currents were removed from each set of traces using the masking tool in Adobe Illustrator. **(B_1-B_3)** Summary data shows the K_{Na} current (mean ± SEM) for each voltage step in VIP-, SST-, and PV-expressing, WT (black and gray) and YH-HET (colors) neurons. The p-values are shown on each graph where $p < 0.05$, and the n values are the number of neurons recorded for each group. **(C_1-C_3)** Plots of the K_{Na} current (mean ± SEM) for each voltage step from -80 to 0 mV in WT (black and gray) and YH-HET (colors) neurons to illustrate the values that are too small to be seen on the graphs in B_1-B_3. The shaded red area in C_2 indicates the subthreshold voltage range with significantly higher K_{Na} currents in YH-HET relative to WT neurons. Statistical significance for I-V plots was tested using Generalized Linear Mixed Models with genotype and voltage step as fixed effects followed by pairwise comparisons at each level.

Supplemental Figure 5-2. Isolation of K_{Na} currents from neurons lacking KCNT1 and KCNT2 channels illustrates the specificity of VU170- vs. TTX-subtraction methods. Voltage steps were applied to voltage-clamped neurons isolated and cultured from *Kcnt1*$^{-/-}$; *Kcnt2*$^{-/-}$ double knockout mice to compare

the delayed outward currents before and after the addition of either 10 µM VU170 or 0.5 µM TTX. **(A)** A summary plot shows the VU-sensitive (red) and TTX-sensitive (grey) difference currents (mean ± SEM) for each voltage step, which were calculated by subtracting the membrane current response to voltage steps (-80 to +50 mV) from a holding potential of -70 mV in VU170 or TTX from the response in control external solution. **(B)** A summary plot of the VU-sensitive (red) and TTX-sensitive (grey) difference currents (mean ± SEM) for each voltage step from -80 to 0 mV to illustrate the values that are too small to be seen on the graph in (A).

Supplemental Figure 6-1. Model VIP and glutamatergic neurons with insertion of SST-like, KCNT1 GOF kinetics show reduced excitability. (A_1) Simulated traces from model VIP neurons, using VIP KCNT1 activation curve parameters (purple) or SST KCNT activation curve parameters (blue), in response to 500-ms current injections at two levels of Na^+-sensitivity (Con-40 mM and GOF-30 mM). Representative traces are shown at increasing current steps from bottom to top for each level. **(A_2)** Summary data from 10 model VIP neurons, with VIP KCNT1 parameters (VIP-Con and VIP-GOF) or SST KCNT1 parameters (SST-GOF) showing (from left to right) the number of APs at different current steps (F-I plot), the input resistance, and rheobase. The bar graphs (mean ± SEM) are overlaid with scatter plots of individual neuron measurements. **(B_1)** Simulated traces from model glutamatergic neurons, using glutamatergic KCNT1 activation curve parameters (green) or SST KCNT activation curve parameters (blue), in response to 500-ms current injections at two levels of Na^+-sensitivity (Con-40 mM and GOF-30 mM). Representative traces are shown at increasing current steps from bottom to top for each level. **(B_2)** Summary data from 10 model glutamatergic neurons, with glutamatergic KCNT1 parameters (Glut-Con and Glut-GOF) or SST KCNT1 parameters (SST-GOF) showing (from left to right) the number of APs at different current steps (F-I plot), the input resistance, and rheobase. The bar graphs (mean ± SEM) are

overlaid with scatter plots of individual neuron measurements. Statistical significance was tested using a Repeated Measures ANOVA. Asterisks indicate where $p < 0.05$ (*), $p \leq 0.01$ (**), and $p \leq 0.001$ (***).

Supplemental Figure 6-2. Model neurons show differential responses to KCNT1 GOF. (A) Bar graphs (mean ± SEM) with overlaid dot plots show the effects of two levels of KCNT1 GOF (Na^+ EC_{50} = 35 or 30 mM) relative to those of control (EC_{50} = 40 mM) on input resistance, rheobase, and AP firing rate at 1.5 × rheobase for GABAergic subtypes (10 model neurons/group). **(B)** Bar graphs (mean ± SEM) with overlaid dot plots show the effects KCNT1 GOF (Na^+ EC_{50} = 30 mM) on VIP GABAergic or glutamatergic model neurons (10/group) with their respective KCNT1 activation curve parameters (VIP-GOF and Glut-GOF) or SST KCNT1 parameters (SST-GOF) relative to those of control (EC_{50} = 40 mM) on input resistance, rheobase, and AP firing rate at 1.5 × rheobase.

Supplemental Figure 7-1. The rate of K_{Na} current block after TTX application is slow relative to I_{NaP} block in GABAergic neurons. Plots show the time course over which I_{NaP} and K_{Na} currents are blocked following 0.5 µM TTX application. Neurons of the labeled type in each panel were voltage clamped and subjected to a slow voltage ramp protocol (20 mV/s over 5 s). TTX (0.5 µM) was applied at time 0 and K_{Na} currents and I_{NaP} were measured on each successive sweep. The K_{Na} current was measured as the normalized difference between each trace and the mean of the pre-TTX current between +20 and +30 mV. I_{NaP} was measured as the normalized difference between each trace and the mean of the pre-TTX current at the 10 mV bracketing the local peak inward current. Once the minimum value was reached for I_{NaP}, all subsequent values were considered zero.

Supplemental Figure 7-2. Model PV neurons show differential responses to KCNT1 GOF with increased I_{NaP}. Bar graphs (mean ± SEM) with overlaid dot plots show the effects of two levels of KCNT1 GOF (Na^+

EC_{50} = 35 or 30 mM), with or without additional I_{NaP}, relative to those of control (EC_{50} = 40 mM) on input resistance, rheobase, and AP firing rate at 1.5 × rheobase for PV neurons (10/group).

Figure 1- Supplemental Table. Electrophysiological parameters of current clamp recordings from neuronal cultures.

	Glutamatergic			FS GABAergic			NFS GABAergic		
	WT	YH-HET		WT	YH-HET		WT	YH-HET	
	N = 9	N = 9		N = 9	N = 9		N = 9	N = 9	
	n = 27	n = 30	p-value	n = 27	n = 29	p-value	n = 26	n = 22	p-value
V_{rest} (mV)	-57.9±1.6	-57.0±1.7	0.61	-53.8±1.8	-52.8±1.8	0.60	-56.3±1.8	-54.4±1.9	0.34
R_{in} (MΩ)	177±17	182±16	0.80	95±9	105±10	0.40	171±16	146±14	0.19
Tau (ms)	32.9±3.8	39.3±4.3	0.14	17.3±2.0	16.7±1.9	0.75	24.9±2.9	22.2±2.7	0.37
C_m (pF)	198±15	215±16	0.23	183±14	163±12	0.15	143±11	164±13	0.09
Rheo (pA)	171±19	148±16	0.25	400±45	415±47	0.78	196±22	297±36	**0.005**
AP_{thresh} (mV)	-28.2±1.5	28.3±1.5	0.93	-25.7±1.6	-25.8±1.6	0.95	-28.2±1.6	-24.4±1.7	**0.012**
AP_{amp} (mV)	77.8±2.0	77.5±1.5	0.51	70.9±1.8	67.8±1.7	0.15	71.5±1.8	68.7±1.9	0.28
AP_{hw} (ms)	2.19±0.12	2.20±0.12	0.95	0.89±0.05	0.91±0.05	0.85	1.36±0.08	1.11±0.07	**0.01**
AHP (mV)	11.8±0.6	11.8±0.6	0.96	27.5±1.3	26.9±1.4	0.78	19.3±1.0	22.6±1.2	**0.034**
AP_{mfr} (Hz)	22.4±2.3	22.4±2.4	0.99	68.8±6.2	71.4±6.6	0.53	35.0±3.8	31.8±3.5	0.25

For an explanation of the parameters, see Methods. R_{in} = input resistance, Tau = membrane time constant, Rheo = rheobase current, C_m = membrane capacitance, AP = action potential, thresh = threshold, amp = amplitude, hw = half width, AHP = afterhyperpolarization, and mfr = maximum firing rate. Values shown are estimated marginal means ± the standard error as determined by implementing a Generalized Linear Mixed Model. P values less than 0.05 are in red, bold type. For each subgroup, N values are the number of mouse pups, and n values are the number of neurons.

Figure 4- Supplemental Table. Electrophysiological parameters of current clamp recordings from neuronal cultures of three major GABAergic subtypes.

	SST$^+$ GABAergic			**VIP$^+$ GABAergic**			**PV$^+$ GABAergic**		
	WT	YH-HET		WT	YH-HET		WT	YH-HET	
	N = 4	N = 5		N = 3	N = 4		N = 3	N = 4	
	n = 45	n = 46	p-value	n = 50	n = 48	p-value	n = 23	n = 25	p-value
R_{in} (MΩ)	133±18	95±13	**0.001**	243±10	249±11	0.645	67±4	66±3	0.850
Tau (ms)	16.9±1.1	13.5±0.8	**0.012**	35.1±2.4	33.1±2.3	0.384	6.7±0.5	6.0±0.4	0.302
C_m (pF)	135±13	152±15	**0.032**	148±6	134±6	0.055	103±5	90±4	0.050
Rheo (pA)	232±41	319±56	**0.001**	149±12	157±13	0.344	546±33	441±24	**0.031**
AP_{thresh} (mV)	-36.4±0.8	-35.2±0.8	0.113	-30.9±0.4	-31.0±0.4	0.850	-34.2±1.8	-35.5±1.9	0.308
AP_{amp} (mV)	79.9±1.5	80.2±1.5	0.850	75.6±0.9	75.5±0.9	0.943	77.6±1.0	82.7±1.0	**0.002**
AP_{hw} (ms)	0.91±0.02	0.86±0.02	0.142	1.09±0.04	1.09±0.04	0.916	0.73±0.03	0.69±0.02	0.180
AHP (mV)	23.0±0.7	23.5±0.7	0.554	17.2±0.9	17.4±0.9	0.860	26.6±0.6	25.3±0.5	0.150
AP_{mfr} (Hz)	57.6±5.1	55.7±4.9	0.432	35.5±2.8	35.9±2.8	0.857	69.4±4.9	79.0±5.3	0.068

For an explanation of the parameters, see Methods. R_{in} = input resistance, Tau = membrane time constant, Rheo = rheobase current, C_m = membrane capacitance, AP = action potential, thresh = threshold, amp = amplitude, hw = half width, AHP = afterhyperpolarization, and mfr = maximum firing rate. Values shown are estimated marginal means ± the standard error as determined by implementing a Generalized Linear Mixed Model. P values less than 0.05 are in red, bold type. For each subgroup, N values are the number of mouse pups, and n values are the number of neurons.

Figure 6- Supplemental Table. Electrophysiological parameters using compartmental model neurons.

Model neuron	Input Resistance (MΩ)	p-value vs 40 mM	Rheobase (pA)	p-value vs 40 mM	AP rate at 1.5x Rheobase (Hz)	p-value vs 40 mM
VIP-40 mM	266.5 ± 28.2		78.7 ± 3.7		7.0 ± 0.7	
VIP-35 mM	266.2 ± 28.1	0.193	79.1 ± 3.6	0.177	7.0 ± 0.7	0.999
VIP-30 mM	264.8 ± 28.0	0.012	80.4 ± 3.5	0.014	6.9 ± 0.7	0.527
VIP-30 mM + SST	260.2 ± 27.8	<0.001	86.3 ± 3.8	<0.001	6.5 ± 0.8	0.011
SST-40 mM	210.3 ± 23.0		127.5 ± 8.5		17.3 ± 2.1	
SST-35 mM	199.9 ± 22.1	0.009	156.3 ± 11.7	<0.001	11.9 ± 2.0	0.025
SST-30 mM	187.1 ± 21.2	0.001	180.0 ± 12.3	<0.001	7.1 ± 1.9	0.003
PV-40 mM	105.8 ± 7.7		258.0 ± 7.5		18.3 ± 1.3	
PV-35 mM	105.5 ± 7.7	0.140	264.5 ± 7.9	0.004	16.8 ± 1.4	0.033
PV-30 mM	103.3 ± 7.5	<0.001	273.0 ± 9.5	0.004	12.4 ± 2.0	0.004
PV-35 mM + I_{NaP}	104.6 ± 7.5	<0.001	238.5 6.3	<0.001	21.1 ± 1.3	<0.001
PV-30 mM + I_{NaP}	103.4 ± 7.4	0.009	250.5 ± 6.9	0.002	20.1 ± 1.5	0.012
Glut-40 mM	147.1 ± 12.0		117.0 ± 10.4		2.46 ± 0.3	
Glut-30 mM	146.4 ± 12.1	0.017	121.5 ± 10.0	<0.001	2.36 ± 0.4	0.593
Glut-30 mM + SST	140.4 ± 11.9	0.001	146.0 ± 9.7	<0.001	1.54 ± 0.3	0.012

For an explanation of the parameters, see Methods. AP = action potential. For each subgroup, 10 model neurons were used and simulations were repeated with the EC_{50} (in mM) for Na^+ for the KCNT1 conductance set at the indicated levels. "+ SST" refers to the activation curve parameters (V_{50} and slope) for the KCNT1 conductance in that neuron type being replaced with those measured in SST neurons. Values shown are means ± the standard error. The statistical test is a repeated measures ANOVA.

REFERENCES

Alcami, P., & Pereda, A. E. (2019). Beyond plasticity: the dynamic impact of electrical synapses on neural circuits. *Nat Rev Neurosci*, *20*(5), 253-271. https://doi.org/10.1038/s41583-019-0133-5

Amitai, Y., Gibson, J. R., Beierlein, M., Patrick, S. L., Ho, A. M., Connors, B. W., & Golomb, D. (2002). The spatial dimensions of electrically coupled networks of interneurons in the neocortex. *J Neurosci*, *22*(10), 4142-4152. https://doi.org/10.1523/JNEUROSCI.22-10-04142.2002

Avermann, M., Tomm, C., Mateo, C., Gerstner, W., & Petersen, C. C. (2012). Microcircuits of excitatory and inhibitory neurons in layer 2/3 of mouse barrel cortex. *J Neurophysiol*, *107*(11), 3116-3134. https://doi.org/10.1152/jn.00917.2011

Barcia, G., Fleming, M. R., Deligniere, A., Gazula, V. R., Brown, M. R., Langouet, M., Chen, H., Kronengold, J., Abhyankar, A., Cilio, R., Nitschke, P., Kaminska, A., Boddaert, N., Casanova, J. L., Desguerre, I., Munnich, A., Dulac, O., Kaczmarek, L. K., Colleaux, L., & Nabbout, R. (2012). De novo gain-of-function KCNT1 channel mutations cause malignant migrating partial seizures of infancy. *Nat Genet*, *44*(11), 1255-1259. https://doi.org/10.1038/ng.2441

Berg, A. P., Sen, N., & Bayliss, D. A. (2007). TrpC3/C7 and Slo2.1 are molecular targets for metabotropic glutamate receptor signaling in rat striatal cholinergic interneurons. *J Neurosci*, *27*(33), 8845-8856. https://doi.org/10.1523/JNEUROSCI.0551-07.2007

Bhattacharjee, A., Gan, L., & Kaczmarek, L. K. (2002). Localization of the Slack potassium channel in the rat central nervous system. *J Comp Neurol*, *454*(3), 241-254. https://doi.org/10.1002/cne.10439

Bonardi, C. M., Heyne, H. O., Fiannacca, M., Fitzgerald, M. P., Gardella, E., Gunning, B., Olofsson, K., Lesca, G., Verbeek, N., Stamberger, H., Striano, P., Zara, F., Mancardi, M. M., Nava, C., Syrbe, S., Buono, S., Baulac, S., Coppola, A., Weckhuysen, S., . . . Rubboli, G. (2021). KCNT1-related epilepsies and epileptic encephalopathies: phenotypic and mutational spectrum. *Brain*, *144*(12), 3635-3650. https://doi.org/10.1093/brain/awab219

Budelli, G., Hage, T. A., Wei, A., Rojas, P., Jong, Y. J., O'Malley, K., & Salkoff, L. (2009). Na+-activated K+ channels express a large delayed outward current in neurons during normal physiology. *Nat Neurosci*, *12*(6), 745-750. https://doi.org/10.1038/nn.2313

Casale, A. E., Foust, A. J., Bal, T., & McCormick, D. A. (2015). Cortical Interneuron Subtypes Vary in Their Axonal Action Potential Properties. *J Neurosci*, *35*(47), 15555-15567. https://doi.org/10.1523/JNEUROSCI.1467-13.2015

Chen, H., Kronengold, J., Yan, Y., Gazula, V. R., Brown, M. R., Ma, L., Ferreira, G., Yang, Y., Bhattacharjee, A., Sigworth, F. J., Salkoff, L., & Kaczmarek, L. K. (2009). The N-terminal domain of Slack determines the formation and trafficking of Slick/Slack heteromeric sodium-activated potassium channels. *J Neurosci*, *29*(17), 5654-5665. https://doi.org/10.1523/JNEUROSCI.5978-08.2009

Cole, B. A., Pilati, N., & Lippiat, J. D. (2021). Epilepsy-causing KCNT1 variants increase $K_{Na}1.1$ channel activity by disrupting the activation gate. *bioRxiv*, 2021.2009.2016.460601. https://doi.org/10.1101/2021.09.16.460601

Connors, B. W. (2017). Synchrony and so much more: Diverse roles for electrical synapses in neural circuits. *Dev Neurobiol*, *77*(5), 610-624. https://doi.org/10.1002/dneu.22493

Davis, G. W. (2013). Homeostatic signaling and the stabilization of neural function. *Neuron*, *80*(3), 718-728. https://doi.org/10.1016/j.neuron.2013.09.044

Debanne, D., Inglebert, Y., & Russier, M. (2019). Plasticity of intrinsic neuronal excitability. *Curr Opin Neurobiol*, *54*, 73-82. https://doi.org/10.1016/j.conb.2018.09.001

Debanne, D., & Russier, M. (2019). The contribution of ion channels in input-output plasticity. *Neurobiol Learn Mem*, *166*, 107095. https://doi.org/10.1016/j.nlm.2019.107095

Dilena, R., DiFrancesco, J. C., Soldovieri, M. V., Giacobbe, A., Ambrosino, P., Mosca, I., Galli, M. A., Guez, S., Fumagalli, M., Miceli, F., Cattaneo, D., Darra, F., Gennaro, E., Zara, F., Striano, P., Castellotti, B., Gellera, C., Varesio, C., Veggiotti, P., & Taglialatela, M. (2018). Early Treatment with Quinidine in 2 Patients with Epilepsy of Infancy with Migrating Focal Seizures (EIMFS) Due to Gain-of-Function KCNT1 Mutations: Functional Studies, Clinical Responses, and Critical Issues for Personalized Therapy. *Neurotherapeutics*, *15*(4), 1112-1126. https://doi.org/10.1007/s13311-018-0657-9

Dudok, B., Klein, P. M., & Soltesz, I. (2022). Toward Understanding the Diverse Roles of Perisomatic Interneurons in Epilepsy. *Epilepsy Curr*, *22*(1), 54-60. https://doi.org/10.1177/15357597211053687

Edelstein, A. D., Tsuchida, M. A., Amodaj, N., Pinkard, H., Vale, R. D., & Stuurman, N. (2014). Advanced methods of microscope control using muManager software. *J Biol Methods*, *1*(2). https://doi.org/10.14440/jbm.2014.36

Evely, K. M., Pryce, K. D., Bausch, A. E., Lukowski, R., Ruth, P., Haj-Dahmane, S., & Bhattacharjee, A. (2017). Slack K(Na) Channels Influence Dorsal Horn Synapses and Nociceptive Behavior. *Mol Pain*, *13*, 1744806917714342. https://doi.org/10.1177/1744806917714342

Favero, M., Sotuyo, N. P., Lopez, E., Kearney, J. A., & Goldberg, E. M. (2018). A Transient Developmental Window of Fast-Spiking Interneuron Dysfunction in a Mouse Model of Dravet Syndrome. *J Neurosci*, *38*(36), 7912-7927. https://doi.org/10.1523/JNEUROSCI.0193-18.2018

Gertler, T. S., Cherian, S., DeKeyser, J. M., Kearney, J. A., & George, A. L., Jr. (2022). K(Na)1.1 gain-of-function preferentially dampens excitability of murine parvalbumin-positive interneurons. *Neurobiol Dis*, *168*, 105713. https://doi.org/10.1016/j.nbd.2022.105713

Gertler, T. S., Thompson, C. H., Vanoye, C. G., Millichap, J. J., & George, A. L., Jr. (2019). Functional consequences of a KCNT1 variant associated with status dystonicus and early-onset infantile encephalopathy. *Ann Clin Transl Neurol*, *6*(9), 1606-1615. https://doi.org/10.1002/acn3.50847

Gibson, J. R., Beierlein, M., & Connors, B. W. (1999). Two networks of electrically coupled inhibitory neurons in neocortex. *Nature*, *402*(6757), 75-79. https://doi.org/10.1038/47035

Gibson, J. R., Beierlein, M., & Connors, B. W. (2005). Functional properties of electrical synapses between inhibitory interneurons of neocortical layer 4. *J Neurophysiol*, *93*(1), 467-480. https://doi.org/10.1152/jn.00520.2004

Grubb, M. S., & Burrone, J. (2010). Activity-dependent relocation of the axon initial segment fine-tunes neuronal excitability. *Nature*, *465*(7301), 1070-1074. https://doi.org/10.1038/nature09160

Hage, T. A., & Salkoff, L. (2012). Sodium-activated potassium channels are functionally coupled to persistent sodium currents. *J Neurosci*, *32*(8), 2714-2721. https://doi.org/10.1523/JNEUROSCI.5088-11.2012

Halabisky, B., Parada, I., Buckmaster, P. S., & Prince, D. A. (2010). Excitatory input onto hilar somatostatin interneurons is increased in a chronic model of epilepsy. *J Neurophysiol*, *104*(4), 2214-2223. https://doi.org/10.1152/jn.00147.2010

Hedrich, U. B., Liautard, C., Kirschenbaum, D., Pofahl, M., Lavigne, J., Liu, Y., Theiss, S., Slotta, J., Escayg, A., Dihne, M., Beck, H., Mantegazza, M., & Lerche, H. (2014). Impaired action potential initiation in GABAergic interneurons causes hyperexcitable networks in an epileptic mouse model carrying a human Na(V)1.1 mutation. *J Neurosci*, *34*(45), 14874-14889. https://doi.org/10.1523/JNEUROSCI.0721-14.2014

Heron, S. E., Smith, K. R., Bahlo, M., Nobili, L., Kahana, E., Licchetta, L., Oliver, K. L., Mazarib, A., Afawi, Z., Korczyn, A., Plazzi, G., Petrou, S., Berkovic, S. F., Scheffer, I. E., & Dibbens, L. M. (2012). Missense mutations in the sodium-gated potassium channel gene KCNT1 cause severe autosomal dominant nocturnal frontal lobe epilepsy. *Nat Genet*, *44*(11), 1188-1190. https://doi.org/10.1038/ng.2440

Hinckley, C. A., Zhu, Z., Chu, J. H., Gubbels, C., Danker, T., Cherry, J. J., Whelan, C. D., Engle, S. J., & Nguyen, V. (2023). Functional evaluation of epilepsy associated KCNT1 variants in multiple cellular systems reveals a predominant gain of function impact on channel properties. *Epilepsia*. https://doi.org/10.1111/epi.17648

Hu, H., & Agmon, A. (2015). Properties of precise firing synchrony between synaptically coupled cortical interneurons depend on their mode of coupling. *J Neurophysiol*, *114*(1), 624-637. https://doi.org/10.1152/jn.00304.2015

Issa, N. P., Nunn, K. C., Wu, S., Haider, H. A., & Tao, J. X. (2023). Putative roles for homeostatic plasticity in epileptogenesis. *Epilepsia*, *64*(3), 539-552. https://doi.org/10.1111/epi.17500

Joiner, W. J., Tang, M. D., Wang, L. Y., Dworetzky, S. I., Boissard, C. G., Gan, L., Gribkoff, V. K., & Kaczmarek, L. K. (1998). Formation of intermediate-conductance calcium-activated potassium channels by interaction of Slack and Slo subunits. *Nat Neurosci*, *1*(6), 462-469. https://doi.org/10.1038/2176

Kim, G. E., Kronengold, J., Barcia, G., Quraishi, I. H., Martin, H. C., Blair, E., Taylor, J. C., Dulac, O., Colleaux, L., Nabbout, R., & Kaczmarek, L. K. (2014). Human slack potassium channel mutations increase positive cooperativity between individual channels. *Cell Rep*, *9*(5), 1661-1672. https://doi.org/10.1016/j.celrep.2014.11.015

Kuba, H., Oichi, Y., & Ohmori, H. (2010). Presynaptic activity regulates Na(+) channel distribution at the axon initial segment. *Nature*, *465*(7301), 1075-1078. https://doi.org/10.1038/nature09087

Kuchenbuch, M., Nabbout, R., Yochum, M., Sauleau, P., Modolo, J., Wendling, F., & Benquet, P. (2021). In silico model reveals the key role of GABA in KCNT1-epilepsy in infancy with migrating focal seizures. *Epilepsia*, *62*(3), 683-697. https://doi.org/10.1111/epi.16834

Lane, B. J., Samarth, P., Ransdell, J. L., Nair, S. S., & Schulz, D. J. (2016). Synergistic plasticity of intrinsic conductance and electrical coupling restores synchrony in an intact motor network. *Elife*, *5*. https://doi.org/10.7554/eLife.16879

Large, A. M., Kunz, N. A., Mielo, S. L., & Oswald, A. M. (2016). Inhibition by Somatostatin Interneurons in Olfactory Cortex. *Front Neural Circuits*, *10*, 62. https://doi.org/10.3389/fncir.2016.00062

Lignani, G., Baldelli, P., & Marra, V. (2020). Homeostatic Plasticity in Epilepsy. *Front Cell Neurosci*, *14*, 197. https://doi.org/10.3389/fncel.2020.00197

Liu, Y., Zhang, F. F., Song, Y., Wang, R., Zhang, Q., Shen, Z. S., Zhang, F. F., Zhong, D. Y., Wang, X. H., Guo, Q., Tang, Q. Y., & Zhang, Z. (2022). The Slack Channel Deletion Causes Mechanical Pain Hypersensitivity in Mice. *Front Mol Neurosci*, *15*, 811441. https://doi.org/10.3389/fnmol.2022.811441

Lu, R., Bausch, A. E., Kallenborn-Gerhardt, W., Stoetzer, C., Debruin, N., Ruth, P., Geisslinger, G., Leffler, A., Lukowski, R., & Schmidtko, A. (2015). Slack channels expressed in sensory neurons control neuropathic pain in mice. *J Neurosci*, *35*(3), 1125-1135. https://doi.org/10.1523/JNEUROSCI.2423-14.2015

Ma, Y., Hu, H., Berrebi, A. S., Mathers, P. H., & Agmon, A. (2006). Distinct subtypes of somatostatin-containing neocortical interneurons revealed in transgenic mice. *J Neurosci*, *26*(19), 5069-5082. https://doi.org/10.1523/JNEUROSCI.0661-06.2006

Magloire, V., Mercier, M. S., Kullmann, D. M., & Pavlov, I. (2019). GABAergic Interneurons in Seizures: Investigating Causality With Optogenetics. *Neuroscientist*, *25*(4), 344-358. https://doi.org/10.1177/1073858418805002

Makinson, C. D., Dutt, K., Lin, F., Papale, L. A., Shankar, A., Barela, A. J., Liu, R., Goldin, A. L., & Escayg, A. (2016). An Scn1a epilepsy mutation in Scn8a alters seizure susceptibility and behavior. *Exp Neurol*, *275 Pt 1*(0 1), 46-58. https://doi.org/10.1016/j.expneurol.2015.09.008

Marder, E., & Goaillard, J. M. (2006). Variability, compensation and homeostasis in neuron and network function. *Nat Rev Neurosci*, *7*(7), 563-574. https://doi.org/10.1038/nrn1949

Markram, H., Muller, E., Ramaswamy, S., Reimann, M. W., Abdellah, M., Sanchez, C. A., Ailamaki, A., Alonso-Nanclares, L., Antille, N., Arsever, S., Kahou, G. A., Berger, T. K., Bilgili, A., Buncic, N., Chalimourda, A., Chindemi, G., Courcol, J. D., Delalondre, F., Delattre, V., . . . Schurmann, F. (2015). Reconstruction and Simulation of Neocortical Microcircuitry. *Cell*, *163*(2), 456-492. https://doi.org/10.1016/j.cell.2015.09.029

Martinez-Espinosa, P. L., Wu, J., Yang, C., Gonzalez-Perez, V., Zhou, H., Liang, H., Xia, X. M., & Lingle, C. J. (2015). Knockout of Slo2.2 enhances itch, abolishes KNa current, and increases action potential firing frequency in DRG neurons. *Elife*, *4*. https://doi.org/10.7554/eLife.10013

McTague, A., Nair, U., Malhotra, S., Meyer, E., Trump, N., Gazina, E. V., Papandreou, A., Ngoh, A., Ackermann, S., Ambegaonkar, G., Appleton, R., Desurkar, A., Eltze, C., Kneen, R., Kumar, A. V., Lascelles, K., Montgomery, T., Ramesh, V., Samanta, R., . . . Kurian, M. A. (2018). Clinical and molecular characterization of KCNT1-related severe early-onset epilepsy. *Neurology*, *90*(1), e55-e66. https://doi.org/10.1212/WNL.0000000000004762

Mikati, M. A., Jiang, Y. H., Carboni, M., Shashi, V., Petrovski, S., Spillmann, R., Milligan, C. J., Li, M., Grefe, A., McConkie, A., Berkovic, S., Scheffer, I., Mullen, S., Bonner, M., Petrou, S., & Goldstein, D. (2015). Quinidine in the treatment of KCNT1-positive epilepsies. *Ann Neurol*, *78*(6), 995-999. https://doi.org/10.1002/ana.24520

Milligan, C. J., Li, M., Gazina, E. V., Heron, S. E., Nair, U., Trager, C., Reid, C. A., Venkat, A., Younkin, D. P., Dlugos, D. J., Petrovski, S., Goldstein, D. B., Dibbens, L. M., Scheffer, I. E., Berkovic, S. F., & Petrou, S. (2014). KCNT1 gain of function in 2 epilepsy phenotypes is reversed by quinidine. *Ann Neurol*, *75*(4), 581-590. https://doi.org/10.1002/ana.24128

Oliva, A. A., Jr., Jiang, M., Lam, T., Smith, K. L., & Swann, J. W. (2000). Novel hippocampal interneuronal subtypes identified using transgenic mice that express green fluorescent protein in GABAergic interneurons. *J Neurosci*, *20*(9), 3354-3368. https://doi.org/10.1523/JNEUROSCI.20-09-03354.2000

Parker, P. R., Cruikshank, S. J., & Connors, B. W. (2009). Stability of electrical coupling despite massive developmental changes of intrinsic neuronal physiology. *J Neurosci*, *29*(31), 9761-9770. https://doi.org/10.1523/JNEUROSCI.4568-08.2009

Pratt, K. G., & Aizenman, C. D. (2007). Homeostatic regulation of intrinsic excitability and synaptic transmission in a developing visual circuit. *J Neurosci*, *27*(31), 8268-8277. https://doi.org/10.1523/JNEUROSCI.1738-07.2007

Quraishi, I. H., Stern, S., Mangan, K. P., Zhang, Y., Ali, S. R., Mercier, M. R., Marchetto, M. C., McLachlan, M. J., Jones, E. M., Gage, F. H., & Kaczmarek, L. K. (2019). An Epilepsy-Associated KCNT1 Mutation Enhances Excitability of Human iPSC-Derived Neurons by Increasing Slack KNa Currents. *J Neurosci*, *39*(37), 7438-7449. https://doi.org/10.1523/JNEUROSCI.1628-18.2019

Reijntjes, D. O. J., Lee, J. H., Park, S., Schubert, N. M. A., van Tuinen, M., Vijayakumar, S., Jones, T. A., Jones, S. M., Gratton, M. A., Xia, X. M., Yamoah, E. N., & Pyott, S. J. (2019). Sodium-activated potassium channels shape peripheral auditory function and activity of the primary auditory neurons in mice. *Sci Rep*, *9*(1), 2573. https://doi.org/10.1038/s41598-019-39119-z

Rizzi, S., Knaus, H. G., & Schwarzer, C. (2016). Differential distribution of the sodium-activated potassium channels slick and slack in mouse brain. *J Comp Neurol*, *524*(10), 2093-2116. https://doi.org/10.1002/cne.23934

Rizzo, F., Ambrosino, P., Guacci, A., Chetta, M., Marchese, G., Rocco, T., Soldovieri, M. V., Manocchio, L., Mosca, I., Casara, G., Vecchi, M., Taglialatela, M., Coppola, G., & Weisz, A. (2016). Characterization of two de novoKCNT1 mutations in children with malignant migrating partial seizures in infancy. *Mol Cell Neurosci*, *72*, 54-63. https://doi.org/10.1016/j.mcn.2016.01.004

Rudy, B., Fishell, G., Lee, S., & Hjerling-Leffler, J. (2011). Three groups of interneurons account for nearly 100% of neocortical GABAergic neurons. *Dev Neurobiol*, *71*(1), 45-61. https://doi.org/10.1002/dneu.20853

Rush, A. M., Dib-Hajj, S. D., Liu, S., Cummins, T. R., Black, J. A., & Waxman, S. G. (2006). A single sodium channel mutation produces hyper- or hypoexcitability in different types of neurons. *Proc Natl Acad Sci U S A*, *103*(21), 8245-8250. https://doi.org/10.1073/pnas.0602813103

Schindelin, J., Arganda-Carreras, I., Frise, E., Kaynig, V., Longair, M., Pietzsch, T., Preibisch, S., Rueden, C., Saalfeld, S., Schmid, B., Tinevez, J. Y., White, D. J., Hartenstein, V., Eliceiri, K., Tomancak, P., & Cardona, A. (2012). Fiji: an open-source platform for biological-image analysis. *Nat Methods*, *9*(7), 676-682. https://doi.org/10.1038/nmeth.2019

Shore, A. N., Colombo, S., Tobin, W. F., Petri, S., Cullen, E. R., Dominguez, S., Bostick, C. D., Beaumont, M. A., Williams, D., Khodagholy, D., Yang, M., Lutz, C. M., Peng, Y., Gelinas, J. N., Goldstein, D. B., Boland, M. J., Frankel, W. N., & Weston, M. C. (2020). Reduced GABAergic neuron excitability, altered synaptic connectivity, and seizures in a KCNT1 gain-of-function mouse model of childhood epilepsy. *Cell Rep*.

Soh, H., Park, S., Ryan, K., Springer, K., Maheshwari, A., & Tzingounis, A. V. (2018). Deletion of KCNQ2/3 potassium channels from PV+ interneurons leads to homeostatic potentiation of excitatory transmission. *Elife*, *7*. https://doi.org/10.7554/eLife.38617

Spitznagel, B. D., Mishra, N. M., Qunies, A. M., Prael, F. J., 3rd, Du, Y., Kozek, K. A., Lazarenko, R. M., Denton, J. S., Emmitte, K. A., & Weaver, C. D. (2020). VU0606170, a Selective Slack Channels Inhibitor, Decreases Calcium Oscillations in Cultured Cortical Neurons. *ACS Chem Neurosci*, *11*(21), 3658-3671. https://doi.org/10.1021/acschemneuro.0c00583

Staley, K. (2015). Molecular mechanisms of epilepsy. *Nat Neurosci*, *18*(3), 367-372. https://doi.org/10.1038/nn.3947

Studtmann, C., Ladislav, M., Topolski, M. A., Safari, M., & Swanger, S. A. (2022). Na(V)1.1 haploinsufficiency impairs glutamatergic and GABAergic neuron function in the thalamus. *Neurobiol Dis*, *167*, 105672. https://doi.org/10.1016/j.nbd.2022.105672

Tai, C., Abe, Y., Westenbroek, R. E., Scheuer, T., & Catterall, W. A. (2014). Impaired excitability of somatostatin- and parvalbumin-expressing cortical interneurons in a mouse model of Dravet syndrome. *Proc Natl Acad Sci U S A*, *111*(30), E3139-3148. https://doi.org/10.1073/pnas.1411131111

Tang, Q. Y., Zhang, F. F., Xu, J., Wang, R., Chen, J., Logothetis, D. E., & Zhang, Z. (2016). Epilepsy-Related Slack Channel Mutants Lead to Channel Over-Activity by Two Different Mechanisms. *Cell Rep*, *14*(1), 129-139. https://doi.org/10.1016/j.celrep.2015.12.019

Taniguchi, H., He, M., Wu, P., Kim, S., Paik, R., Sugino, K., Kvitsiani, D., Fu, Y., Lu, J., Lin, Y., Miyoshi, G., Shima, Y., Fishell, G., Nelson, S. B., & Huang, Z. J. (2011). A resource of Cre driver lines for genetic targeting of GABAergic neurons in cerebral cortex. *Neuron*, *71*(6), 995-1013. https://doi.org/10.1016/j.neuron.2011.07.026

Ting, J. T., Daigle, T. L., Chen, Q., & Feng, G. (2014). Acute brain slice methods for adult and aging animals: application of targeted patch clamp analysis and optogenetics. *Methods Mol Biol*, *1183*, 221-242. https://doi.org/10.1007/978-1-4939-1096-0_14

Tran, C. H., Vaiana, M., Nakuci, J., Somarowthu, A., Goff, K. M., Goldstein, N., Murthy, P., Muldoon, S. F., & Goldberg, E. M. (2020). Interneuron Desynchronization Precedes Seizures in a Mouse Model of Dravet Syndrome. *J Neurosci*, *40*(13), 2764-2775. https://doi.org/10.1523/JNEUROSCI.2370-19.2020

Tremblay, R., Lee, S., & Rudy, B. (2016). GABAergic Interneurons in the Neocortex: From Cellular Properties to Circuits. *Neuron*, *91*(2), 260-292. https://doi.org/10.1016/j.neuron.2016.06.033

Turrigiano, G. (2011). Too many cooks? Intrinsic and synaptic homeostatic mechanisms in cortical circuit refinement. *Annu Rev Neurosci*, *34*, 89-103. https://doi.org/10.1146/annurev-neuro-060909-153238

Turrigiano, G. (2012). Homeostatic synaptic plasticity: local and global mechanisms for stabilizing neuronal function. *Cold Spring Harb Perspect Biol*, *4*(1), a005736. https://doi.org/10.1101/cshperspect.a005736

Urban-Ciecko, J., & Barth, A. L. (2016). Somatostatin-expressing neurons in cortical networks. *Nat Rev Neurosci*, *17*(7), 401-409. https://doi.org/10.1038/nrn.2016.53

Varghese, N., Moscoso, B., Chavez, A., Springer, K., Ortiz, E., Soh, H., Santaniello, S., Maheshwari, A., & Tzingounis, A. V. (2023). KCNQ2/3 Gain-of-Function Variants and Cell Excitability: Differential Effects in CA1 versus L2/3 Pyramidal Neurons. *J Neurosci*, *43*(38), 6479-6494. https://doi.org/10.1523/JNEUROSCI.0980-23.2023

Wengert, E. R., Miralles, R. M., Wedgwood, K. C. A., Wagley, P. K., Strohm, S. M., Panchal, P. S., Idrissi, A. M., Wenker, I. C., Thompson, J. A., Gaykema, R. P., & Patel, M. K. (2021). Somatostatin-Positive Interneurons Contribute to Seizures in SCN8A Epileptic Encephalopathy. *J Neurosci*, *41*(44), 9257-9273. https://doi.org/10.1523/JNEUROSCI.0718-21.2021

Wu, J., Quraishi, I. H., Zhang, Y., Bromwich, M., & Kaczmarek, L. K. (2024). Disease-causing Slack potassium channel mutations produce opposite effects on excitability of excitatory and inhibitory neurons. *Cell Rep*, *43*(3), 113904. https://doi.org/10.1016/j.celrep.2024.113904

Yang, J., & Prescott, S. A. (2023). Homeostatic regulation of neuronal function: importance of degeneracy and pleiotropy. *Front Cell Neurosci*, *17*, 1184563. https://doi.org/10.3389/fncel.2023.1184563

Yu, F. H., Mantegazza, M., Westenbroek, R. E., Robbins, C. A., Kalume, F., Burton, K. A., Spain, W. J., McKnight, G. S., Scheuer, T., & Catterall, W. A. (2006). Reduced sodium current in GABAergic interneurons in a mouse model of severe myoclonic epilepsy in infancy. *Nat Neurosci*, *9*(9), 1142-1149. https://doi.org/10.1038/nn1754

Zhang, J., Chen, X., Eaton, M., Wu, J., Ma, Z., Lai, S., Park, A., Ahmad, T. S., Que, Z., Lee, J. H., Xiao, T., Li, Y., Wang, Y., Olivero-Acosta, M. I., Schaber, J. A., Jayant, K., Yuan, C., Huang, Z., Lanman, N. A., . . . Yang, Y. (2021). Severe deficiency of the voltage-gated sodium channel Na(V)1.2 elevates neuronal excitability in adult mice. *Cell Rep*, *36*(5), 109495. https://doi.org/10.1016/j.celrep.2021.109495

Zhang, Q., Gao, S. H., Shen, Z. S., Wang, Y., Hu, S. W., Duan, G. B., Liu, Y., Zhong, D. Y., Liu, J., Sun, M. H., Zhang, X., Cao, T. Y., Cao, J. L., Tang, Q. Y., & Zhang, Z. (2022). The Slack Channel Regulates Anxiety-Like Behaviors via Basolateral Amygdala Glutamatergic Projections to Ventral Hippocampus. *J Neurosci*, *42*(14), 3049-3064. https://doi.org/10.1523/JNEUROSCI.2027-21.2022

Figure 1

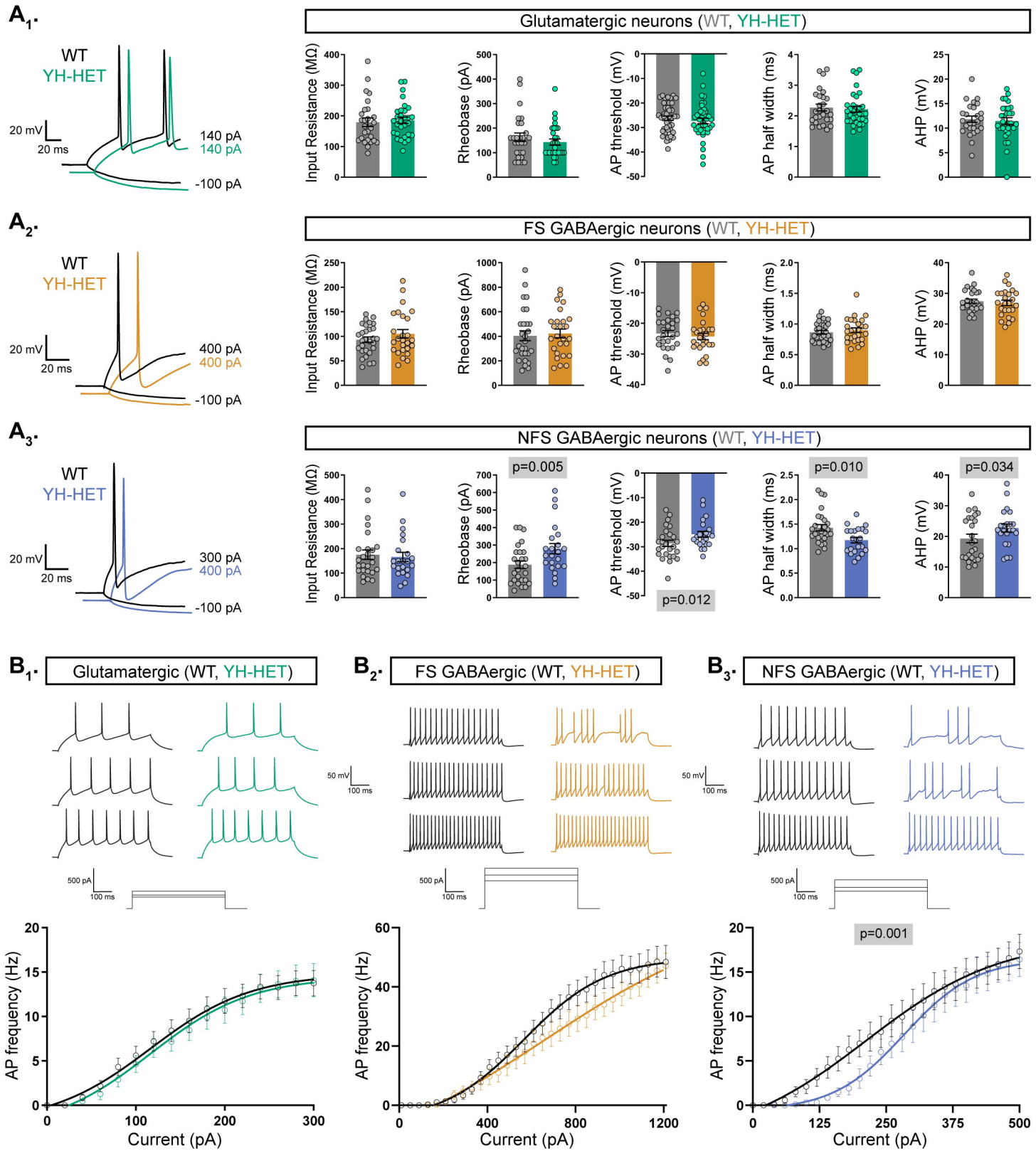
A1.
WT
YH-HET
20 mV
20 ms
140 pA
140 pA
-100 pA
Glutamatergic neurons (WT, YH-HET)
Input Resistance (MΩ)
Rheobase (pA)
AP threshold (mV)
AP half width (ms)
AHP (mV)
A2.
WT
YH-HET
20 mV
20 ms
400 pA
400 pA
-100 pA
FS GABAergic neurons (WT, YH-HET)
Input Resistance (MΩ)
Rheobase (pA)
AP threshold (mV)
AP half width (ms)
AHP (mV)
A3.
WT
YH-HET
20 mV
20 ms
300 pA
400 pA
-100 pA
NFS GABAergic neurons (WT, YH-HET)
Input Resistance (MΩ)
Rheobase (pA)
p=0.005
AP threshold (mV)
p=0.012
AP half width (ms)
p=0.010
AHP (mV)
p=0.034
B1.
Glutamatergic (WT, YH-HET)
50 mV
100 ms
500 pA
100 ms
AP frequency (Hz)
Current (pA)
B2.
FS GABAergic (WT, YH-HET)
50 mV
100 ms
500 pA
100 ms
AP frequency (Hz)
Current (pA)
B3.
NFS GABAergic (WT, YH-HET)
50 mV
100 ms
500 pA
100 ms
p=0.001
AP frequency (Hz)
Current (pA)

Figure 2

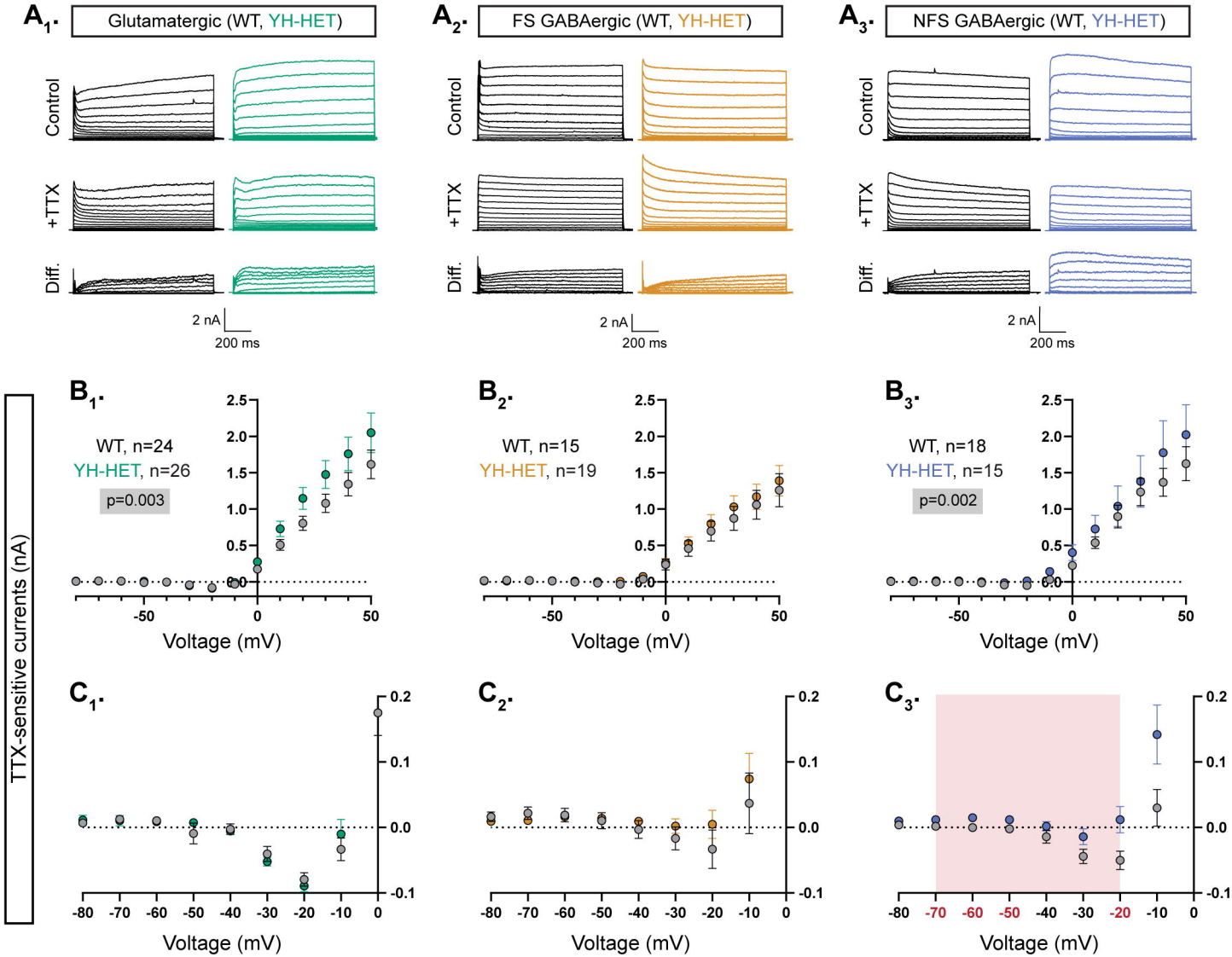
A1.
Glutamatergic (WT, YH-HET)
A2.
FS GABAergic (WT, YH-HET)
A3.
NFS GABAergic (WT, YH-HET)
Control
+TTX
Diff.
2 nA
200 ms
B1.
WT, n=24
YH-HET, n=26
p=0.003
B2.
WT, n=15
YH-HET, n=19
B3.
WT, n=18
YH-HET, n=15
p=0.002
Voltage (mV)
TTX-sensitive currents (nA)
C1.
C2.
C3.

Figure 3

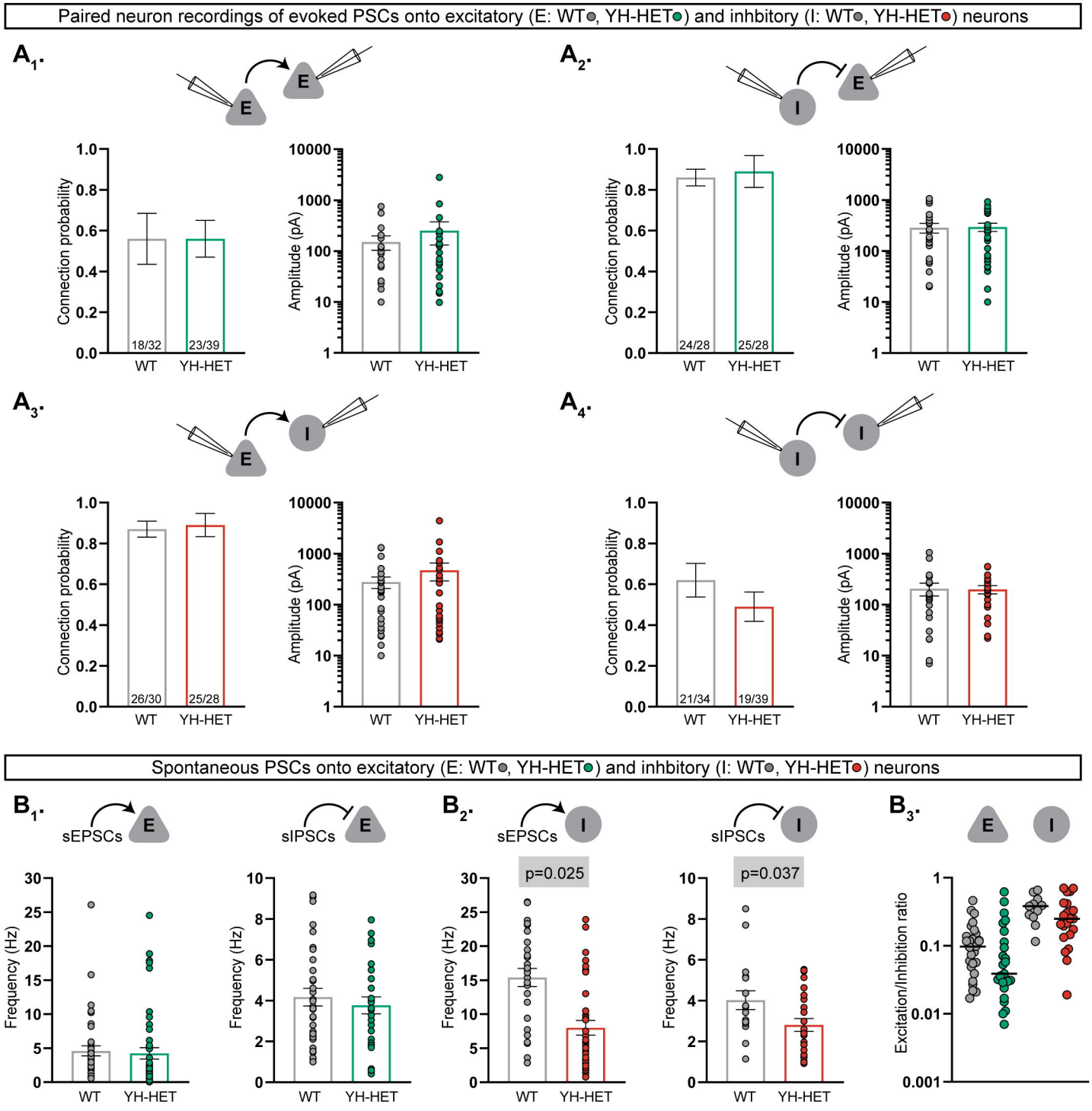
Paired neuron recordings of evoked PSCs onto excitatory (E: WT, YH-HET) and inhbitory (I: WT, YH-HET) neurons
A1.
A2.
A3.
A4.
E
I
Connection probability
Amplitude (pA)
18/32
23/39
24/28
25/28
26/30
25/28
21/34
19/39
WT
YH-HET
Spontaneous PSCs onto excitatory (E: WT, YH-HET) and inhbitory (I: WT, YH-HET) neurons
B1.
B2.
B3.
sEPSCs
sIPSCs
Frequency (Hz)
p=0.025
p=0.037
Excitation/Inhibition ratio

Figure 4

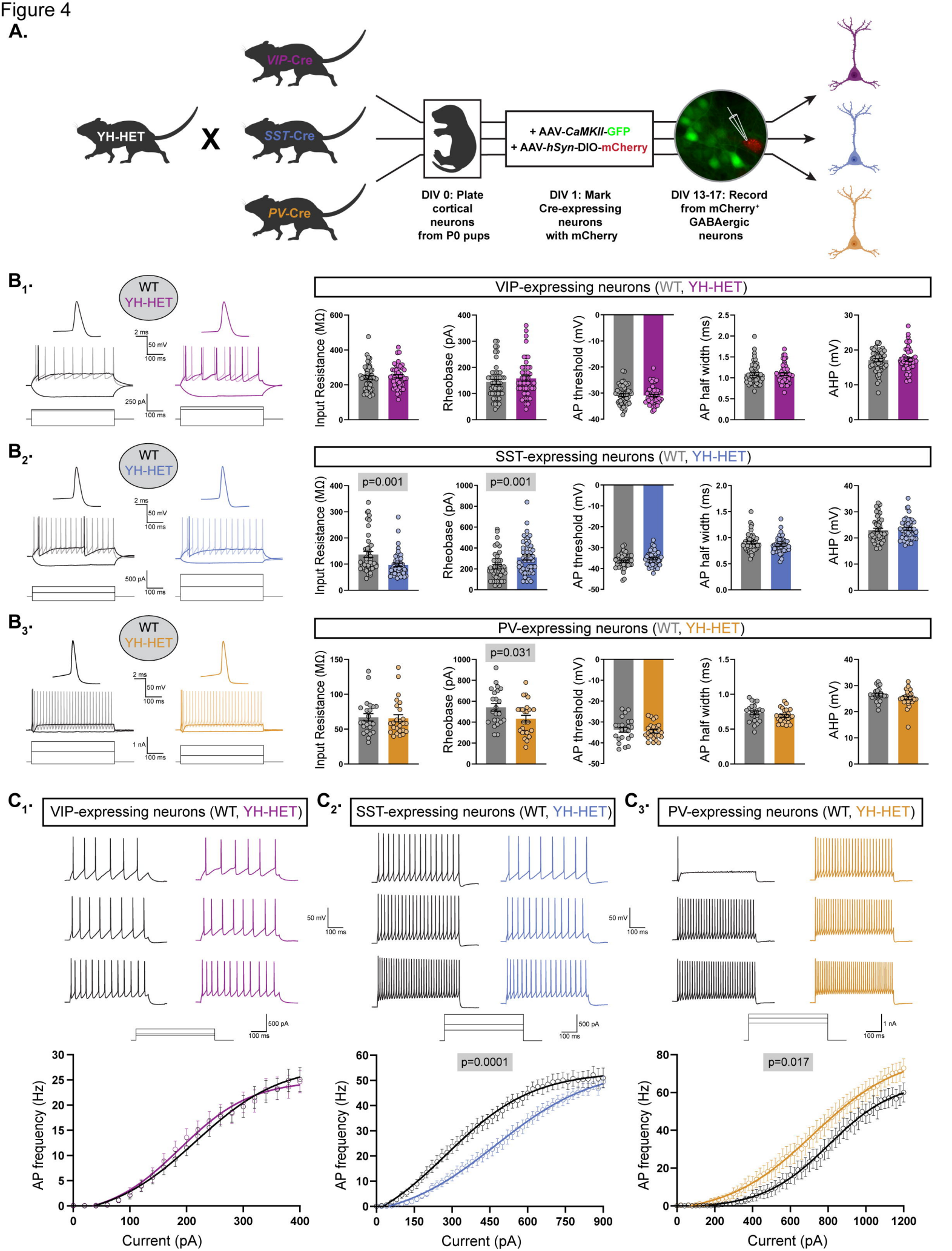
A.
YH-HET
X
VIP-Cre
SST-Cre
PV-Cre
+ AAV-CaMKII-GFP
+ AAV-hSyn-DIO-mCherry
DIV 0: Plate cortical neurons from P0 pups
DIV 1: Mark Cre-expressing neurons with mCherry
DIV 13-17: Record from mCherry+ GABAergic neurons
B1.
WT
YH-HET
VIP-expressing neurons (WT, YH-HET)
Input Resistance (MΩ)
Rheobase (pA)
AP threshold (mV)
AP half width (ms)
AHP (mV)
B2.
SST-expressing neurons (WT, YH-HET)
p=0.001
p=0.001
B3.
PV-expressing neurons (WT, YH-HET)
p=0.031
C1.
VIP-expressing neurons (WT, YH-HET)
C2.
SST-expressing neurons (WT, YH-HET)
C3.
PV-expressing neurons (WT, YH-HET)
AP frequency (Hz)
Current (pA)
p=0.0001
p=0.017

Figure 5

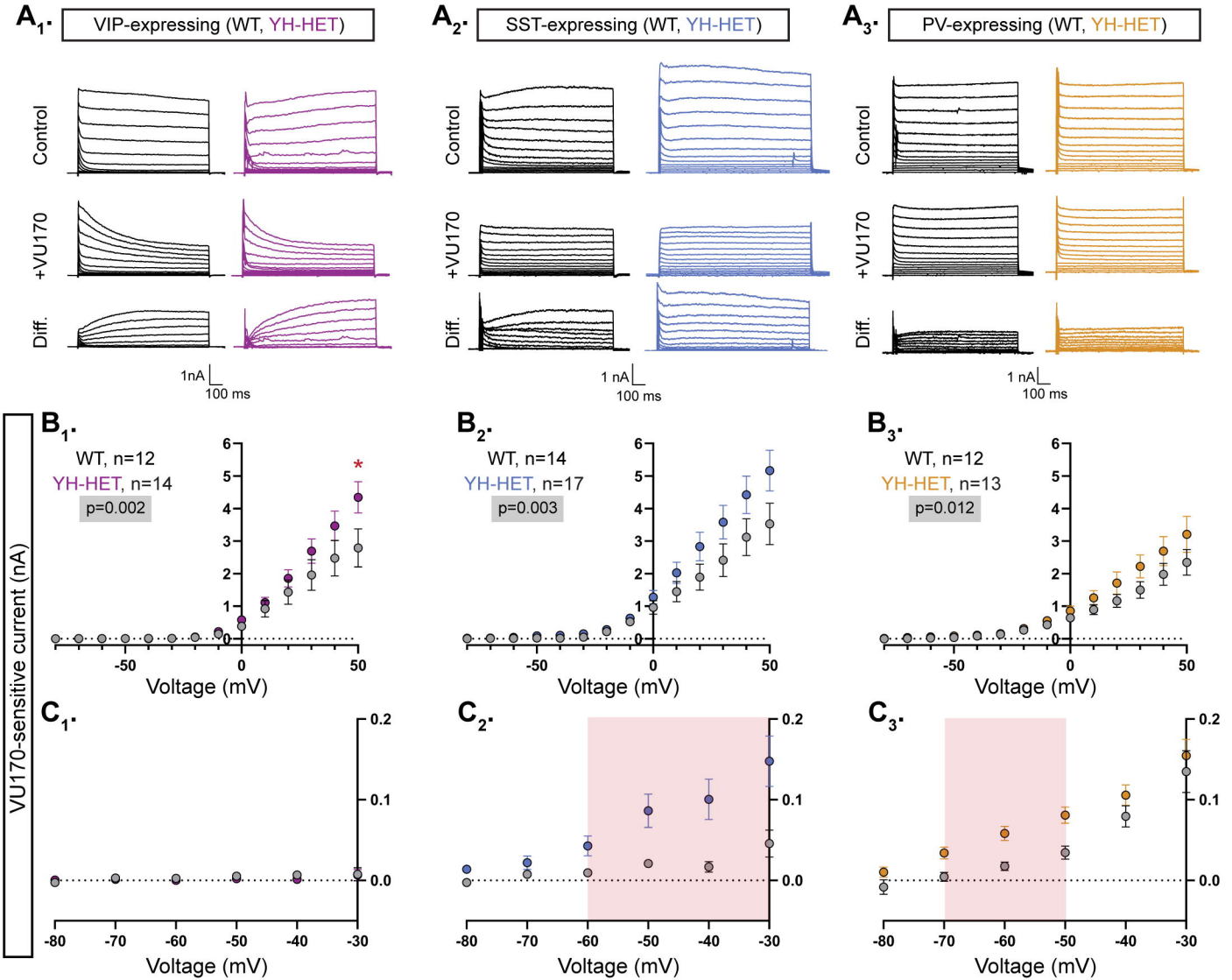
A1.
VIP-expressing (WT, YH-HET)
A2.
SST-expressing (WT, YH-HET)
A3.
PV-expressing (WT, YH-HET)
Control
+VU170
Diff.
1nA
100 ms
1 nA
100 ms
1 nA
100 ms
VU170-sensitive current (nA)
B1.
WT, n=12
YH-HET, n=14
p=0.002
B2.
WT, n=14
YH-HET, n=17
p=0.003
B3.
WT, n=12
YH-HET, n=13
p=0.012
Voltage (mV)
C1.
C2.
C3.
Voltage (mV)

Figure 6

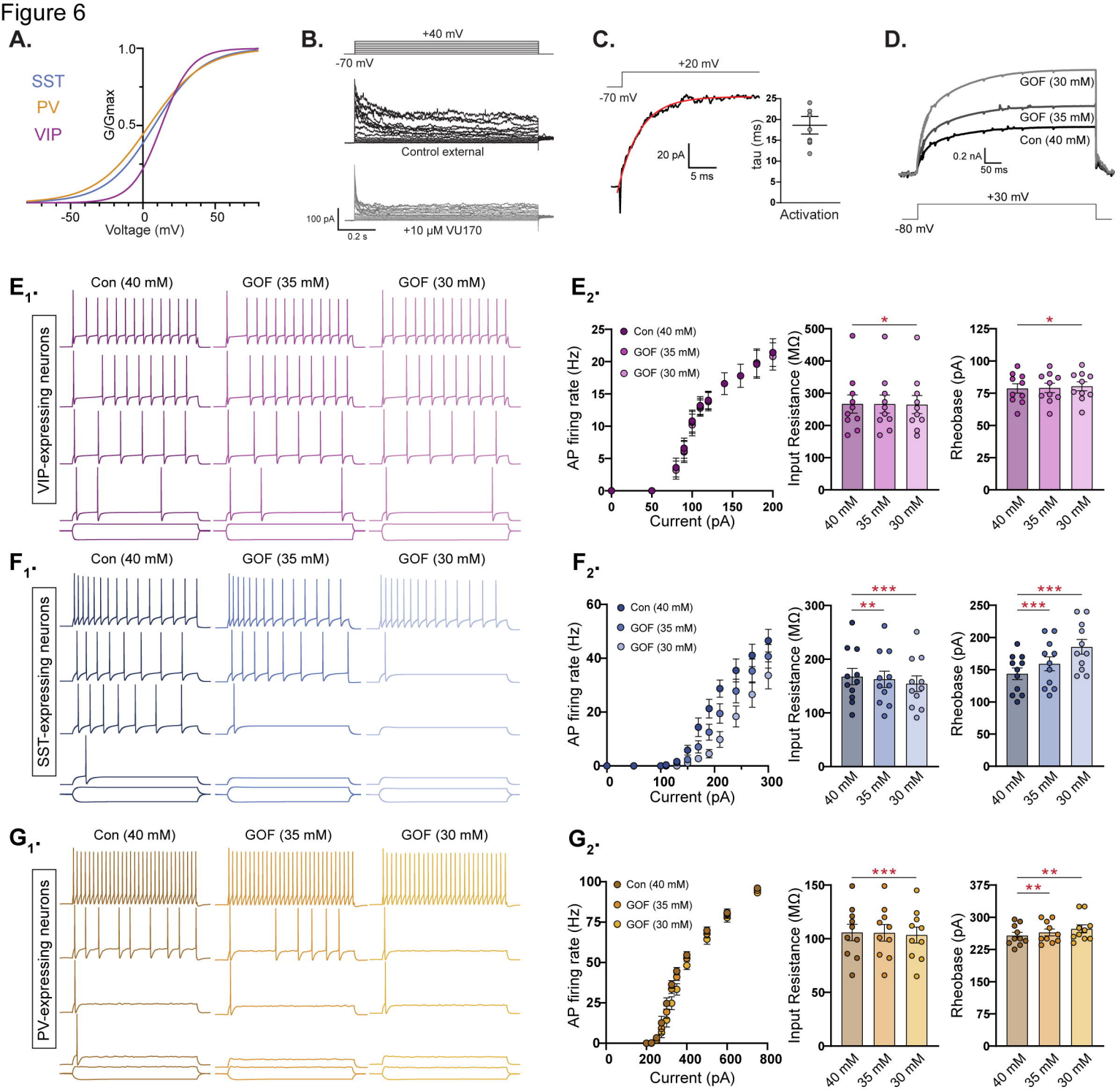
A.
SST
PV
VIP
G/Gmax
Voltage (mV)
B.
+40 mV
-70 mV
Control external
100 pA
0.2 s
+10 μM VU170
C.
+20 mV
-70 mV
20 pA
5 ms
tau (ms)
Activation
D.
GOF (30 mM)
GOF (35 mM)
Con (40 mM)
0.2 nA
50 ms
+30 mV
-80 mV
E1.
Con (40 mM)
GOF (35 mM)
GOF (30 mM)
VIP-expressing neurons
E2.
AP firing rate (Hz)
Current (pA)
Input Resistance (MΩ)
Rheobase (pA)
40 mM
35 mM
30 mM
F1.
SST-expressing neurons
F2.
G1.
PV-expressing neurons
G2.

Figure 7

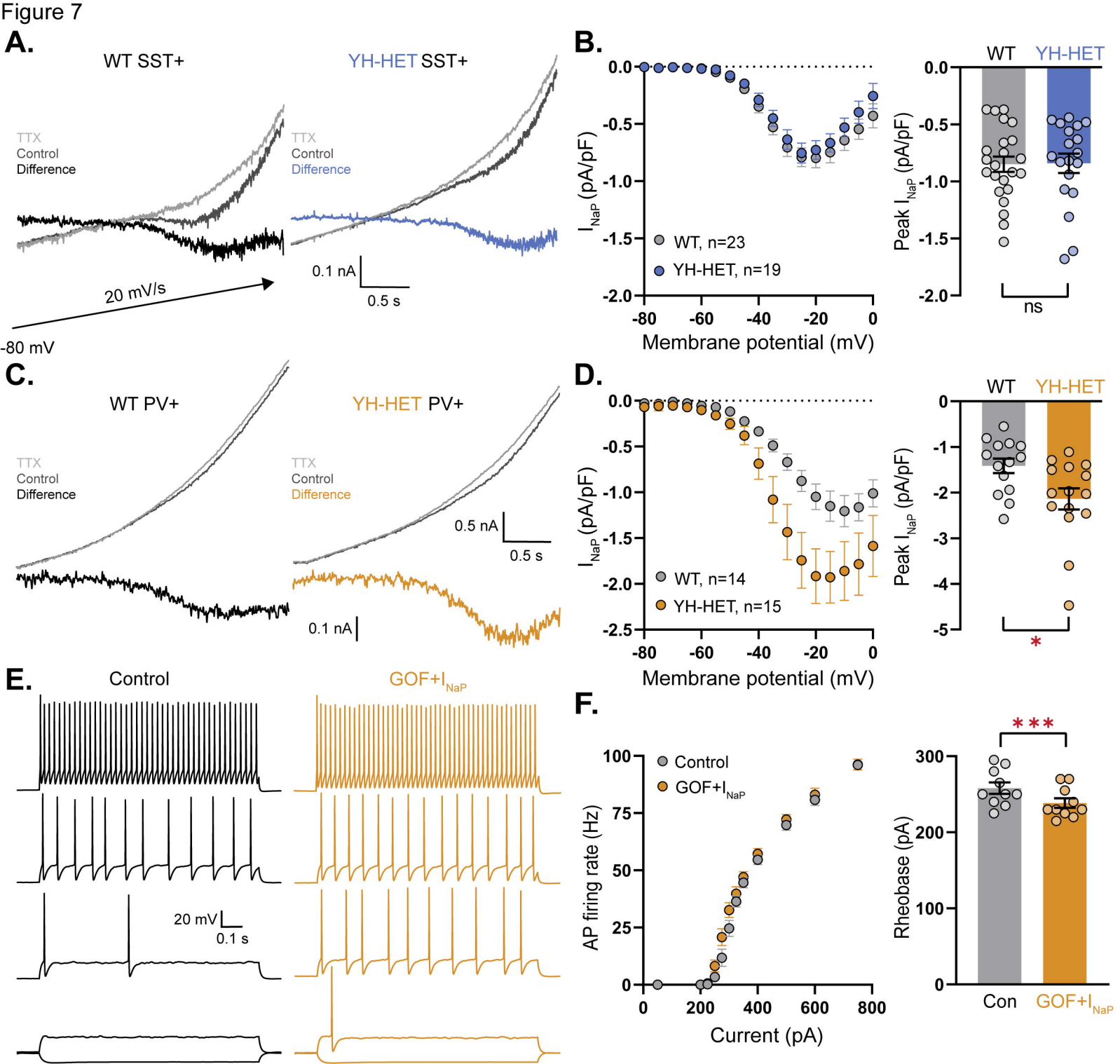
A.
WT SST+
YH-HET SST+
TTX
Control
Difference
20 mV/s
-80 mV
0.1 nA
0.5 s
B.
WT, n=23
YH-HET, n=19
Membrane potential (mV)
Peak I_NaP (pA/pF)
WT
YH-HET
ns
C.
WT PV+
YH-HET PV+
0.5 nA
0.5 s
0.1 nA
D.
WT, n=14
YH-HET, n=15
*
E.
Control
GOF+I_NaP
20 mV
0.1 s
F.
AP firing rate (Hz)
Current (pA)
Rheobase (pA)
***
Con

Figure 8

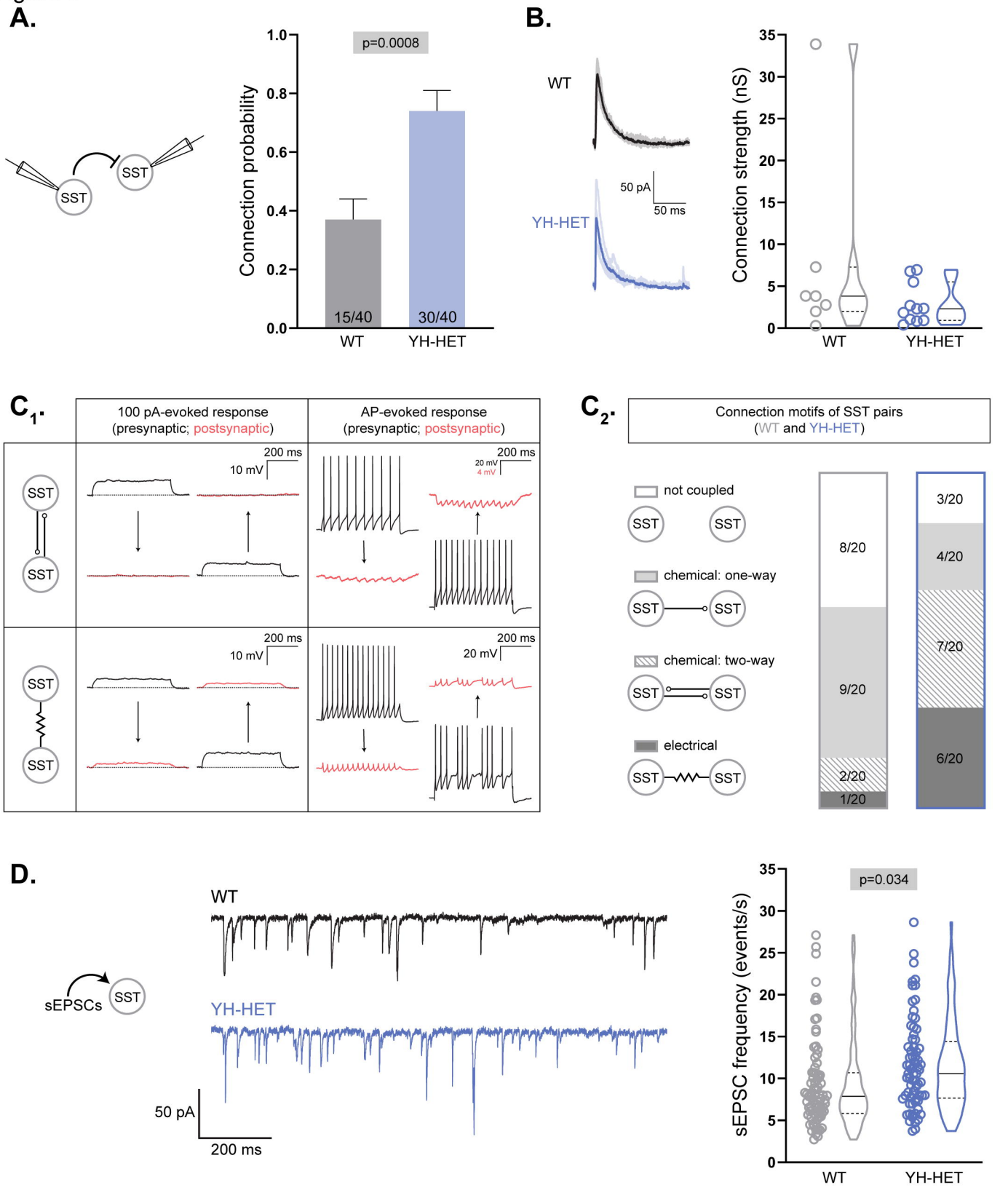
A.
SST
SST
p=0.0008
Connection probability
1.0
0.8
0.6
0.4
0.2
0.0
15/40
30/40
WT
YH-HET
B.
WT
YH-HET
50 pA
50 ms
Connection strength (nS)
35
30
25
20
15
10
5
0
WT
YH-HET
C1.
100 pA-evoked response
(presynaptic; postsynaptic)
AP-evoked response
(presynaptic; postsynaptic)
200 ms
10 mV
20 mV
4 mV
SST
SST
C2.
Connection motifs of SST pairs
(WT and YH-HET)
not coupled
chemical: one-way
chemical: two-way
electrical
8/20
9/20
2/20
1/20
3/20
4/20
7/20
6/20
D.
sEPSCs
SST
WT
YH-HET
50 pA
200 ms
p=0.034
sEPSC frequency (events/s)
35
30
25
20
15
10
5
0
WT
YH-HET

Figure 9
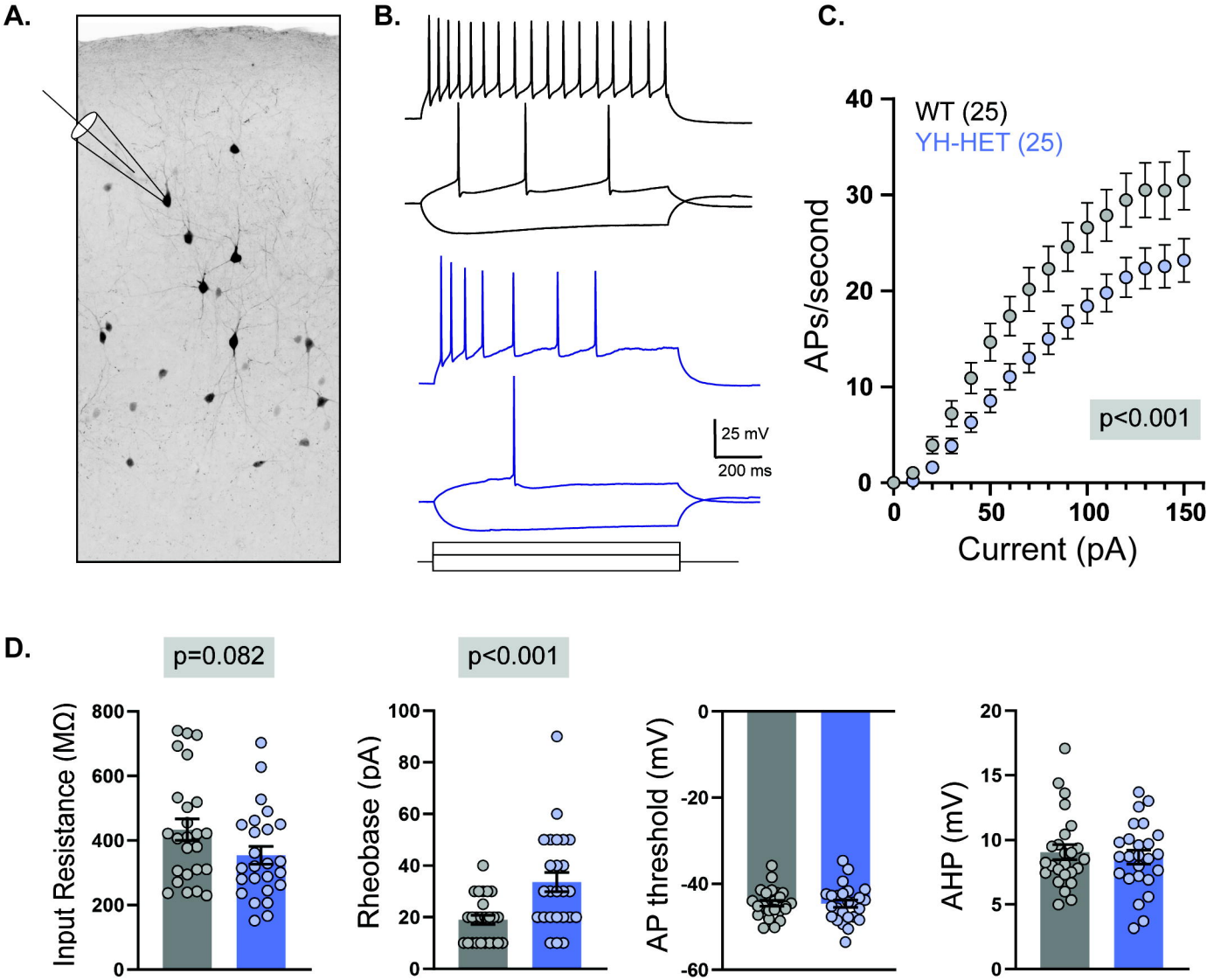
GFP-expressing GIN neurons (WT, YH-HET)